Decomposing oceanic temperature and salinity change using ocean carbon change

Charles E. Turner[1], Peter J. Brown[2], Kevin I. C. Oliver[1], and Elaine L. McDonagh[2,3]

[1]University of Southampton, European Way, Southampton, SO14 3ZH
[2]National Oceanography Centre, European Way, Southampton, SO14 3ZH
[3]NORCE Norwegian Research Centre, Bjerknes Centre for Climate Research, Bergen, Norway

Correspondence: Charles Turner (charles.turner@soton.ac.uk)

Abstract. As the planet warms due to the accumulation of anthropogenic CO_2 in the atmosphere, the interaction of surface ocean carbonate chemistry and the radiative forcing of atmospheric CO_2 leads to the global ocean sequestering heat and carbon, in a ratio that is near constant in time. This ratio has been approximated as globally uniform, enabling the intimately linked patterns of ocean heat and carbon uptake to be derived. Patterns of ocean salinity also change as the earth system warms due to hydrological cycle intensification and perturbations to air-sea freshwater fluxes. Local temperature and salinity change in the ocean may result from perturbed air-sea fluxes of heat and freshwater (excess temperature, salinity), or from reorganisation of the preindustrial temperature and salinity fields (redistributed temperature, salinity), which are largely due to circulation changes. Here, we present a novel method in which the redistribution of preindustrial carbon is diagnosed, and the redistribution of temperature and salinity estimated using only local spatial information. We demonstrate this technique in the NEMO OGCM coupled to the MEDUSA-2 Biogeochemistry model under a RCP8.5 scenario over 1860-2099. The excess changes (difference between total and redistributed property changes) are thus calculated. We demonstrate that a global ratio between excess heat and temperature is largely appropriately regionally with key regional differences consistent with reduced efficiency in the transport of carbon through the mixed layer base at high latitudes. On centennial timescales, excess heat increases everywhere, with 25±2% of annual global heat uptake in the North Atlantic over the 21st century. Excess salinity meanwhile increases in the Atlantic but is generally negative in other basins, consistent with increasing atmospheric transport of freshwater out of the Atlantic. In the North Atlantic, changes in the inventory of excess salinity are detectable in the late 19th century, whereas increases in the inventory of excess heat does not become significant until the early 21st century. This is consistent with previous studies which find salinification of the Subtropical North Atlantic to be an early fingerprint of anthropogenic climate change.

Over the full simulation, we also find the imprint of AMOC slowdown through significant redistribution of heat away from the North Atlantic, and of salinity to the South Atlantic. Globally, temperature change at 2000m is accounted for both by redistributed and excess heat, but for salinity the excess component accounts for the majority of changes at the surface and at depth. This indicates that the circulation variability contributes significantly less to changes in ocean salinity than to heat content.

By the end of the simulation excess heat is the largest contribution to density change and steric sea level rise, while excess salinity greatly reduces spatial variability in steric sea level rise through density compensation of excess temperature patterns, particularly in the Atlantic. In the Atlantic, redistribution of the preindustrial heat and salinity fields also produce generally compensating changes in sea level, though this compensation is less clear elsewhere.

The regional strength of excess heat and salinity signal grows through the model run in response to the evolving forcing. In addition, the regional strength of the redistributed temperature and salinity signals also grow, indicating increasing circulation variability or systematic circulation change on timescales of at least the model run.

1 Introduction

As a result of continuing anthropogenic CO_2 emissions, atmospheric CO_2 levels continue to increase, as well as global mean surface air temperatures. However, the ocean acts to mitigate both changes, having absorbed a third of all CO_2 emissions to date (Khatiwala et al., 2013), as well as over 93% of the additional heat accumulating in the Earth system (Church et al., 2011). Though this greatly slows the rate of surface warming, it is not without consequence: as a result of the excess heat content, global sea levels are expected to rise significantly over the coming centuries, in large part due to the thermal expansion of seawater (thermosteric sea level rise) (Pardaens et al., 2011), (Church et al., 2013), with enormous implications for future economic development (Hinkel et al., 2014). It also has important implications for the future of marine ecosystem health: ocean warming has a direct effect on marine life as a driver of deoxygenation (Oschlies et al., 2018), as well as through increased stratification (Gruber, 2011). The uptake of carbon similarly affects marine life through its role in ocean acidification (Gruber, 2011).

As a result of the interaction of ocean biogeochemistry with rising atmospheric CO_2 and the increased radiative forcing it generates, there exists a near linear relationship between global mean surface air temperature change and cumulative carbon emissions, known as the Transient Climate Response to cumulative Carbon Emissions (TCRE) (Goodwin et al., 2015), (Katavouta et al., 2018). A similar near-linear global relationship exists between increases in ocean heat and carbon content (Bronselaer and Zanna, 2020), which can be observed at a range of scales: both increases in global ocean heat and carbon inventories, and in local ocean temperature and carbon are linearly related.

Local ocean heat content changes are contributed to by both the addition or removal of heat from the surface due to perturbed radiative forcing (excess heat), or from the rearrangement of the preindustrial temperature field from circulation variability (redistributed heat). Ocean salinity changes can also result from perturbations to air-sea freshwater fluxes (excess salinity), or due to the rearrangement of the preindustrial salinity field (redistributed salinity).

The redistribution of temperature and salinity as a result of ocean circulation variability acts on much shorter timescales than the accumulation of excess heat and salinity. Circulation-related variability comprises the majority of temporal variability in contemporary ocean temperature and salinity, (Bindoff and Mcdougall, 1994), (Desbruyères et al., 2017) and regional sea level (Church et al., 2013). However, the excess component is anticipated to dominate in the future (Bronselaer and Zanna

(2020), Zika et al. (2021)). Thus the evolution of excess temperature and patterns of excess salinity as well as changes in ocean circulation comprise a key source of uncertainty in estimates of regional sea level rise (Church et al., 2013).

While it remains challenging to separate excess and redistributed (preindustrial) heat, a similar decomposition for carbon is widely used. Identifying whether changes in ocean dissolved inorganic carbon (DIC) content are due to increased atmospheric CO_2 or changes in other processes (circulation, biological change, etc.) is possible due to the fact that atmospheric CO_2 can considered to be globally uniform, and biogeochemically-driven DIC changes may be parameterised. This allows us to separate changes in DIC into changes in anthropogenic carbon (C_{anth}, the DIC content considered to be due to increased atmospheric CO_2), and changes in natural carbon (C_{nat}, defined to be the non-C_{anth} part of DIC) (Gruber et al. (1996), Hall et al. (2002), Touratier and Goyet (2004), Khatiwala et al. (2005), Vázquez-Rodríguez et al. (2009)). Natural carbon is therefore the sum of the pools of saturation carbon, carbonate carbon, soft tissue carbon and disequilibrium carbon: it can be thought of as the DIC field which exists in the ocean, prior to the Industrial Revolution (Williams and Follows (2011)), McKinley et al. (2017), Couldrey et al. (2019)). Although not precisely identical, the decomposition of DIC into natural and anthropogenic components can provide valuable insights into excess and redistributed carbon (Williams et al., 2021). Unlike carbon however, it is not straightforward to separate anthropogenically-driven changes in ocean temperature or salinity, due to the non-globally uniform nature of the perturbations: this has motivated a variety of techniques which aim to decompose excess and redistributed heat content changes.

One approach to determine excess temperature is to use a Passive Anomalous Tracer (PAT), which obeys the same physics as temperature, but is defined to have a preindustrial field which is zero everywhere: the preindustrial field therefore cannot contribute to redistribution (Banks and Gregory (2006), Gregory et al. (2016)), and so PAT reveals the distribution and evolution of the excess temperature field. Alternatively, it is possible in simulations to force ocean circulation to obey preindustrial dynamics despite increasing radiative forcing: this gives a similar result, though differing by a second order term to the PAT implementation (Winton et al., 2013).

While these methods have been very informative they are only applicable to models: no real world PAT tracer exists and while transient tracers such as chlorofluorocarbons are a close analogue their interpretation in terms of excess temperature necessitates the determination of a excess temperature boundary condition. This motivates the development of proxy methods, which aim to diagnose the excess and redistributed temperature from other tracers and might be more generally applied. The approach of Bronselaer and Zanna (2020) is an example of this: by approximating the distribution of excess temperature with that of anthropogenic carbon, they are able to leverage the mechanistic coupling relating excess heat accumulation to anthropogenic carbon accumulation to produce estimates of the scale and patterns of excess heat uptake.

Using an alternative carbon based methodology, Williams et al. (2021) explains differences in storage of heat and carbon in terms of two components: 1) the correlation of excess heat and carbon (both increase over time), and 2) anticorrelation of redistributed heat and carbon (the preindustrial distributions of temperature and carbon are inverted due to the inverse temperature dependence of carbon dioxide solubility). They use this to diagnose excess and redistributed heat (note Williams et al. (2021) refer to this as added heat, though the definitions used are identical). Bronselaer and Zanna (2020) can therefore be thought of as specifying the character of this positive correlation between excess heat and anthropogenic carbon, in order to estimate excess heat directly from anthropogenic carbon. Here, we introduce an approach which builds on this, specifying the character of the anticorrelation between redistributed heat and natural carbon locally via the preindustrial ocean state. This allows us to estimate redistributed heat (and other parameters) directly from redistributed carbon, which we approximate using natural carbon. As natural carbon is strongly anticorrelated with temperature throughout the ocean, and can be usefully assumed to change only due to redistribution, it is an ideal tracer with which to estimate temperature redistribution.

The benefit of this approach is that specifying the character of the relationship between the excess components of temperature and DIC change, as done by Bronselaer and Zanna (2020), relies on a global biogeochemical relationship derived from the radiative forcing of CO_2 and the ocean carbon buffer factor: making it only applicable to temperature. In contrast, in the absence of mixing, redistribution leaves the properties of a parcel of water unchanged. As a result, a redistribution first approach is more generally applicable, which allows us to not only produce estimates of temperature redistribution, but also new estimates of salinity, and by extension density, redistribution. Using these, we investigate the patterns of storage of excess and redistributed temperature and salinity by the global ocean.

2 Data and Methods

2.1 Model set up

We use the NEMO v3.2 OGCM (Ocean General Circulation Model) (Madec, 2008) coupled to the MEDUSA-2 biogeochemical model (Yool et al., 2013) and the Louvain-la-Neuve (LIM2) dynamic sea ice model (Timmermann et al., 2005). The model was configured with the ORCA1 grid with a nominal 1 degree resolution and 64 vertical levels (Madec and Imbard, 1996). The model was spun up for 900 years, before three 240 year simulations spanning 1860-2099 were spawned: a control run (CTR), coupled climate change run (COU), and a ‘warming only’ run (RAD), following the convention of Schwinger et al. (2014), Rodgers et al. (2020). The ocean model was forced with output from the HadGEM2-ES (Collins et al., 2011), an earth system model driven using prescribed greenhouse gas, land use and atmospheric chemistry forcing following the RCP8.5 scenario over the 1860-2099 time period. In this scenario, atmospheric CO_2 increases to over 900ppm by the end of the simulations (Riahi et al. (2011), atmospheric CO_2 in these simulations is shown in Couldrey et al. (2016), Figure 1a). Surface heat, momentum, freshwater fluxes, and atmospheric chemistry from HadGEM2-ES were used to force NEMO at 6 hourly intervals, and no restoring was used.

The CTR run is forced with the 8 repetitions of the first 30 years of these fluxes from the HadGEM2-ES forcing, with a fixed atmospheric CO_2 of 286ppm: no significant climate change occurs in these 30 years. The 900 year spinup for all 3 model runs was also forced using this 30 year repeat forcing.

The COU run is forced with the full 240 year output from HadGEM2-ES. The RAD run has the same physical variability as in COU including that driven by atmospheric carbon increases but the atmospheric carbon is artificially relaxed to preindustrial conditions. As the RAD run only includes changes in DIC due to physical change (circulation change and warming), rather than the ocean biogeochemical response to increased atmospheric CO_2, we can calculate this response, namely anthropogenic carbon or $\mathrm{C_{anth}}$, directly from the difference of the COU and RAD runs:

$$\mathrm{C_{anth}}(x,y,z,t) = \mathrm{DIC^{COU}}(x,y,z,t) - \mathrm{DIC^{RAD}}(x,y,z,t) \tag{1}$$

Natural carbon, or $\mathrm{C_{nat}}$, is then defined to be the total DIC content with the anthropogenic carbon contribution removed: it is therefore calculated as

$$\mathrm{C_{nat}} = \mathrm{DIC^{COU}} - \mathrm{C_{anth}} - \Delta\mathrm{DIC^{CTR}} = \mathrm{DIC^{RAD}} - \Delta\mathrm{DIC^{CTR}}, \tag{2}$$

where $\Delta\mathrm{DIC^{CTR}}$ is control run drift, equivalent to $\mathrm{DIC^{CTR}}(x,y,z,t) - \mathrm{DIC^{CTR}}(x,y,z,t_0)$, where t_0 is the beginning of the three simulations, 1860. Therefore by definition all DIC is natural carbon at the beginning of our simulations, as the DIC fields are identical at the beginning of all 3 runs. DIC changes are then the sum of natural and anthropogenic carbon change. As such, we decompose the local DIC content at any time in the following way (note as $\mathrm{C_{anth}}$ is defined to be zero at time t_0 $\mathrm{C_{anth}} = \Delta\mathrm{C_{anth}}$ here):

$$\mathrm{DIC}(x,y,z,t) = \mathrm{DIC}(x,y,z,t_0) + \Delta\mathrm{C_{nat}}(x,y,z,t) + \mathrm{C_{anth}}(x,y,z,t) \tag{3}$$

Changes in natural carbon, $\Delta\mathrm{C_{nat}}$, are thus given by the difference in DIC between the RAD and CTR runs:

$$\Delta\mathrm{C_{nat}} = \mathrm{DIC^{RAD}} - \mathrm{DIC^{CTR}} \tag{4}$$

For further detail on model setup, see Couldrey et al. (2016) and Couldrey et al. (2019): we utilise the same simulations as these papers. We also note that Couldrey et al. (2019) compared the representation of DIC and alkalinity in these models runs to GLODAPv2 observations (Lauvset et al., 2016), finding the modelled carbon cycle to be representative of observations, and so we expect our carbon derived identification of excess temperature and salinity to also be representative.

2.2 Relating the redistribution of temperature and carbon

Following Williams et al. (2021), the preindustrial temperature and carbon fields of the ocean are anticorrelated as a result of the strong inverse temperature dependence of carbon solubility. In contrast, the excess temperature and anthropogenic carbon fields are correlated due to the radiative forcing of atmospheric $\mathrm{CO_2}$. Bronselaer and Zanna (2020) specify this correlation between excess heat and anthropogenic carbon using a time varying, globally uniform constant, which they refer to as the carbon-heat coupling or α. Here, we aim to similarly relate the redistribution of temperature and natural carbon using an analogous redistribution coefficient, which we will label κ_r. As we also decompose salinity, we will use superscripts to denote the variable we are relating to natural carbon: the temperature redistribution coefficient,κ_r^T, refers to the preindustrial spatial covariability of natural carbon and temperature, whereas the salinity redistribution coefficient, κ_r^S refers to the preindustrial spatial covariability of natural carbon and salinity. Decomposing the total temperature change,

$$\Delta\Theta(x,y,z,t) = \Delta\Theta_e(x,y,z,t) + \Delta\Theta_r(x,y,z,t), \tag{5}$$

where Θ is in situ potential temperature, Δ refers to change since 1860, and the subscripts e and r refer to the excess and redistributed components, respectively.

The approach of Bronselaer and Zanna (2020) is therefore to parameterise $\Delta\Theta_e$ as

$$\Delta\Theta_e(x,y,z,t) = \alpha_T(\Delta t) \times \mathrm{C}_{\mathrm{anth}}(x,y,z,t), \tag{6}$$

where α_T is their coefficient α, expressed in units of temperature rather than heat. α is estimated as the ratio of global heat to DIC accumulation, over the time period $\Delta t = t - t_0$, where t_0 is a preindustrial time (1860 here). Similarly, we might parameterise the redistribution of temperature, $\Delta\Theta_r$ in terms of the natural carbon change:

$$\Delta\Theta_r(x,y,z,t) \approx \kappa_r^T(x,y,z) \times \Delta\mathrm{C}_{\mathrm{nat}}(x,y,z,t) \tag{7}$$

Unlike α_T, κ_r^T is not a function of time: it is instead a function of position, as it relates the spatial covariability of the preindustrial temperature and carbon fields at a given point. This method is equally applicable to any property for which we aim to estimate redistribution although each property pair will have a distinct distribution of κ_r: we could instead choose to relate the spatial covariability of the preindustrial salinity and carbon fields. We would therefore estimate redistributed salinity, ΔS_r, as

$$\Delta S_r(x,y,z,t) \approx \kappa_r^S(x,y,z) \times \Delta\mathrm{C}_{\mathrm{nat}}(x,y,z,t), \tag{8}$$

In Equations 7 and 8, no constraint is made such that the global integral of redistributed heat is zero (or equivalently the global mean redistributed temperature is zero). If $\mathrm{C}_{\mathrm{nat}}$ were a perfect tracer for redistribution, then its global integral would be zero. However, we expect the global integral of $\Delta\mathrm{C}_{\mathrm{nat}}$ to be nonzero, predominantly as a result of the outgassing of saturation carbon, $\mathrm{C}_{\mathrm{sat}}$ (the DIC content of the ocean resulting from equilibrium with the preindustrial atmosphere), in response to ocean warming. Thus the quantities $\Delta\mathrm{DIC}_r$ (redistributed DIC) and $\Delta\mathrm{C}_{\mathrm{nat}}$ will differ, particularly over timescales of multiple decades to centuries (Williams et al., 2021): to reflect this, we have used approximate rather than exact equality in Equations 7 and 8. In general, when integrating over the global ocean,

$$\frac{d}{dt}\iiint \mathrm{C}_{\mathrm{nat}} dV < 0, \tag{9}$$

so we correct for the divergence of $\mathrm{C}_{\mathrm{nat}}$ and the ideal behaviour of a redistributed preindustrial carbon field using a repartitioning factor, which we refer to as γ. We refer to the corrected quantity as adjusted natural carbon, $\mathrm{C}_{\mathrm{nat}}^{\mathrm{adj}}$. We use this to repartition a fraction of anthropogenic carbon into the adjusted natural carbon in order to correct for $\mathrm{C}_{\mathrm{sat}}$ outgassing.

This repartitioning allows us to force the global integral of adjusted natural carbon changes to zero. However, because globally integrated biology driven changes in $\mathrm{C}_{\mathrm{nat}}$ may be nonzero, we instead enforce the condition that globally integrated redistributed heat, not adjusted natural carbon, is zero. We therefore estimate the redistributed temperature field as

$$\Delta\Theta_r(x,y,z,t) = \kappa_r^T(x,y,z) \times \Delta\mathrm{C}_{\mathrm{nat}}^{\mathrm{adj}}(x,y,z,t) = \kappa_r^T(x,y,z) \times \Big(\Delta\mathrm{C}_{\mathrm{nat}}(x,y,z,t) + \gamma(t)\mathrm{C}_{\mathrm{anth}}(x,y,z,t)\Big) \tag{10}$$

where $\gamma(t)$ is a factor between 0 and 1 such that over the global ocean

$$\iiint \Delta\Theta_r dV = 0 \tag{11}$$

at all times. γ must be less than 1 or $\mathrm{C}_{\mathrm{nat}}^{\mathrm{adj}}$ would exceed DIC, and so would not be physically meaningful. It is constrained to be positive as historically, atmospheric CO_2 has increased from preindustrial levels and so the global $\mathrm{C}_{\mathrm{anth}}$ inventory is positive. However, if the global $\mathrm{C}_{\mathrm{anth}}$ inventory were negative, γ could also be negative (though greater than -1).

As with redistributed temperature, we will estimate redistributed salinity as

$$\Delta S_r(x,y,z,t) = \kappa_r^S(x,y,z) \times \Delta \mathrm{C}_{\mathrm{nat}}^{\mathrm{adj}}(x,y,z,t) = \kappa_r^S(x,y,z) \tag{12}$$

We also note that we may combine Equations 10 and 12 in order to directly estimate salinity redistribution from temperature redistribution and vice versa. This follows from the property that (absent mixing) redistribution does not alter the properties of a parcel of water, and so the redistribution of natural carbon, temperature and salinity are related by the spatial covariability of their preindustrial fields. Alternatively, we may observe that the choice of $\mathrm{C}_{\mathrm{nat}}$ is not unique as a tracer for which to estimate redistribution: as we previously note, we only a require a tracer which can be considered to change only through redistribution. The sum of the preindustrial temperature or salinity fields and their redistributed components both satisfy this, and so can be used to estimate redistribution of other tracers themselves.

We now wish to estimate our redistribution coefficients relating the change in adjusted natural carbon to changes in temperature (κ_r^T) and salinity (κ_r^S), in order to determine their redistribution. To do this, we use a statistical method, examining how the model temperature or salinity and $\mathrm{C}_{\mathrm{nat}}$ fields covary on subdecadal timescales in order to estimate the covariability of their preindustrial state. It is well known that when making repeated observations at a fixed spatial location, the majority of observed changes in temperature and salinity are due to circulation variability, rather than material changes in water mass properties on subdecadal timescales (for example Bindoff and Mcdougall (1994), Firing et al. (2017)). We exploit the dominance of circulation variability on these timescales, assuming that the correlation between deviations in temperature, salinity and DIC from their mean state on subdecadal timescales are due entirely to circulation variability. The correlations obtained allow us to estimate how circulation acts to couple changes in temperature and salinity to changes in natural carbon, at every point in the ocean.

The calculation is performed as follows: in each grid cell, we use the first 100 years (1860-1959) of yearly mean temperature, salinity and DIC from our CTR run, binned into 10 decades. In each decadal bin, the mean tracer (Θ or S and $\mathrm{C}_{\mathrm{nat}}$) values are subtracted, giving yearly Θ, S and $\mathrm{C}_{\mathrm{nat}}$ anomalies from the decadal mean in that grid cell. We perform this decadal binning in order to preclude the possibility of any excess temperature or excess DIC contaminating our relationship as the result of models drifts or surface forcing driven variability due to the 30 year repeated forcing: though these effects should be small, they are both partitioned by the excess/redistribution decomposition into excess.

The correlations between the yearly anomalies from decadal means, for the entire 100 years of data, are then used to establish an intermediate value, which we label κ_i, at each grid cell. This is done using a total least squares linear fit, implemented as two dimensional PCA: we estimate κ_i as the gradient of the slope obtained. We perform a total least squares fit, rather than ordinary, as we expect the two variables to be correlated, but not causally: total least squares is therefore more appropriate, as our relationship should not be affected by the choice of dependent variable.

We then calculate a suppression factor, ϕ, based on the quality of the correlations to estimate κ_r for each variable: this process is detailed in Appendix (A), along with a visualisation of the estimation process. As with κ_r, this will be unique to each variable. ϕ is designed such that where the correlations we obtain between the Θ or S and $\mathrm{C_{nat}}$ anomalies from decadal means are poor or nonexistent, no estimate of redistribution is made. As a result of this, if local $\mathrm{C_{nat}}$ changes due to biological processes but temperature or salinity due to circulation variability, our method will misclassify this as excess temperature or salinity: this also will occur at maxima/minima of temperature or salinity. However, due to the implementation of our γ correction, these misclassifications will globally integrate to zero. Over the full simulation, adjusted natural carbon increases by approximately 2μmol/kg, 0.1% of the mean preindustrial DIC concentration. This implies the net global divergence of $\mathrm{C_{nat}^{adj}}$ and $\Delta\mathrm{DIC}_r$ is approximately 0.1%.

The full calculation is therefore performed as

$$\Delta\Theta_r(x,y,z,t) = \kappa_r^T(x,y,z) \times \Delta\mathrm{C_{nat}^{adj}}(x,y,z,t) = \phi_\Theta(x,y,z) \times \kappa_i^T(x,y,z) \times \Delta\mathrm{C_{nat}^{adj}}(x,y,z,t) \tag{13}$$

for temperature, and

$$\Delta S_r(x,y,z,t) = \kappa_r^S(x,y,z) \times \Delta\mathrm{C_{nat}^{adj}}(x,y,z,t) = \phi_S(x,y,z) \times \kappa_i^S(x,y,z) \times \Delta\mathrm{C_{nat}^{adj}}(x,y,z,t) \tag{14}$$

for salinity.

Estimates of redistributed salinity are complicated in the top 200m by the impacts of freshwater dilution, leading to misattribution of excess salinity from freshwater fluxes to redistribution. To resolve this issue, we recalculate salinity redistribution using the same statistical approach to locally estimate the salinity redistribution from the redistributed temperature field: we refer to this as a two step estimation. This calculation is performed as

$$\Delta S_r^2(x,y,z,t) = \kappa_r^{T-S}(x,y,z) \times \Delta\Theta_r(x,y,z,t) = \kappa_r^{T-S}(x,y,z) \times \phi_T(x,y,z) \times \kappa_i^T(x,y,z) \times \Delta\mathrm{C_{nat}^{adj}}(x,y,z,t) \tag{15}$$

where the superscript 2 in $\Delta S_r^2(x,y,z,t)$ refers to the two step estimation. κ_r^{T-S} is an estimate of the T-S curve angle, and is estimated in the same way as κ_i^T and κ_i^S: we do not apply a new suppression factor.

The two redistributed salinity estimates were then combined using a sigmoidal weighting, exchanging from the two step estimate at the surface to the one step estimate at depth with equal weight at 200m. This was not found to leave any artefacts in the estimates of salinity redistribution. This process is detailed in Appendix (B).

For temperature, approximately 80% of grid cells globally have a scale factor of 0.8-1, and we find by the end of our run, the suppression factor ϕ alters the redistributed temperature of 93% grid cells globally by less than 0.04 degrees, and 60% by less than 0.02 degrees, though the RMS mean redistributed temperature is reduced by 5%. However, the small number of grid cells producing extremely large estimates (10's of degrees of change) are effectively suppressed. We therefore estimate that the statistical nature of our method introduces a minimum uncertainty of approximately 5% into our inventories.

γ was calculated for each year using Equation (10) to satisfy Equation (11): a fraction of $\mathrm{C_{anth}}$ was added to $\mathrm{C_{nat}}$ to ensure the global integral of redistributed heat is zero in each year, with the fraction representing the γ value that year. We then smooth the value of γ over a 10 year period, before adding the fraction of $\mathrm{C_{anth}}$ each year given by our smoothed γ value to $\mathrm{C_{nat}}$ to obtain our $C_{\rm nat}^{\rm adj}$ field. Over the 240 year run, γ increases from 0 to approximately 0.12, with an approximately sigmoid shape. This is shown in Appendix (C).

Once the $C_{\rm nat}^{\rm adj}$ field had been built, it was used to generate both the redistributed temperature and salinity fields: we did not recalculate a new γ value to force a zero integral of salinity redistribution in our salinity decomposition. This approach was chosen for 3 reasons. Calculating a new γ for salinity would mean a new $C_{\rm nat}^{\rm adj}$ field, and so the evolution of the redistributed temperature and salinity fields would not be linked by the same adjusted $C_{\rm nat}^{\rm adj}$ field. In addition, the salinity of sea ice in the model (6PSU) and reduced carbon content of sea ice causes some ice melt to be captured as redistributed salinity, rather than excess. This means that we do not expect globally integrated salinity redistribution to sum to zero as we do for temperature. Finally, as globally integrated redistributed salinity is not independently constrained to be zero, this allows us to use this global integral as a check on the validity of the method.

Excess and redistributed density fields were then built from the decomposed temperature and salinity fields. To do this, the redistributed fields were added to the initial fields, and redistributed density calculated using TEOS-10 (McDougall and Barker, 2011). Initial density was then subtracted for density redistribution. Excess density fields were then calculated as the difference between the redistributed density field and the total density change.

3 Results

3.1 Methodology Validation

We validate our results by comparison with previous carbon proxy based methods. The method of Bronselaer and Zanna (2020) relies on the assumption of a globally uniform α value, linking carbon and heat changes at all scales, which they refer to as the carbon-heat coupling. In comparison, our technique does not enforce global uniformity of this carbon-heat coupling: a local carbon-heat coupling, $\Delta\Theta_e/\Delta C_{\rm anth}$, is instead an output of our method. Henceforth, we will refer to the global mean carbon-heat coupling as α_T, and the local carbon-heat coupling as $\Delta\Theta_e/\Delta C_{\rm anth}$: specifically, the local carbon-heat coupling links the anthropogenic carbon and excess heat.

As we expect the correlations between the excess components of temperature and DIC changes to be positive, and between the redistributed components of temperature and DIC changes to be negative, we can infer whether our technique reliably estimates excess heat by comparing histograms of correlations between the different components of temperature and carbon change. To do this, we compare the total temperature change to DIC change, the excess temperature change to $C_{\rm anth}$ change, and the redistributed temperature change to $C_{\rm nat}^{\rm adj}$ change (equivalent to κ_r^T in our method), for each grid cell at depths of less than 2000m in our simulations. We exclude depths greater than 2000m due to the negligible ventilation and $C_{\rm anth}$ beyond this depth horizon. The total change and excess component correlations are calculated as the ratio of decadal mean temperature and carbon at each grid cell for the period 2090-2099 minus the initial values in 1860. Assuming the assumption of a globally uniform α_T to be accurate, we expect to find a broad distribution of ratios of total temperature change to DIC change with both positive and negative correlations, and a narrower distribution of ratios of excess temperature change to $C_{\rm anth}$ change,

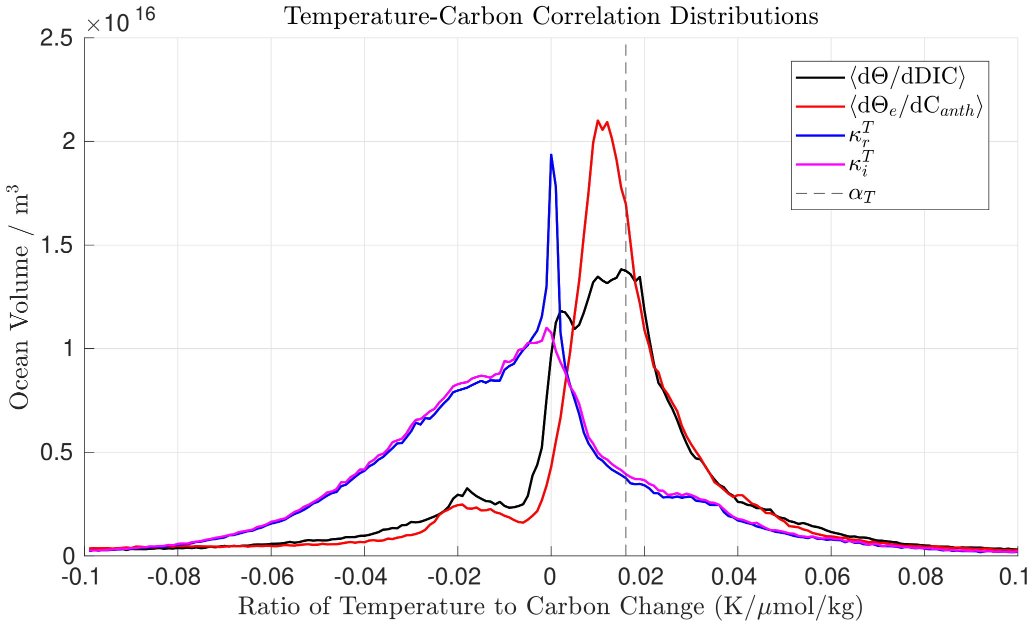

Figure 1. Histograms of the distribution of correlations relating different components of the temperature and carbon fields, over the full simulation (1860-2099). The global mean value α_T is shown by the dashed line. We include both the final redistribution coefficient, κ_r^T (blue), and its intermediate estimate, κ_i^T (magenta), as well as the ratio of total temperature change to DIC change ($\langle d\Theta/d\mathrm{DIC}\rangle$, black), and local excess temperature to anthropogenic carbon change ($\langle d\Theta_e/d\mathrm{C}_{\mathrm{anth}}\rangle$, red).

centred about the global mean value α_T. We also expect the correlations between redistributed temperature changes and $\mathrm{C}_{\mathrm{nat}}^{\mathrm{adj}}$ to generally be negative.

This is shown in Figure 1: the volume weighted histogram of each of these quantities over the upper 2000m of the ocean. The distribution of the ratio of total temperature change to DIC change (black line) is generally positive, indicating the dominance of excess temperature and DIC over redistribution over this time period and region, but is broad and encompasses both positive and negative values. Its peak value occurs at the global mean value α_T: 0.016K/μmol/kg. The peak value of the ratio of excess temperature change to $\mathrm{C}_{\mathrm{anth}}$ accumulation (red line) displays a slightly lower peak value (0.012-0.014K/μmol/kg), but this peak is approximately 50% greater than that of total change ($2.1 \times 10^{16}\mathrm{m}^3$ vs $1.4 \times 10^{16}\mathrm{m}^3$). This implies that the assumption of a globally uniform carbon-heat coupling, α, is broadly appropriate although a large spread in values exists, and that our method reliably identifies excess heat.

The distribution of the ratio of redistributed temperature change to $\mathrm{C}_{\mathrm{nat}}^{\mathrm{adj}}$ change (κ_r^T, blue line), is also generally negative, as expected, with a much broader distribution than the distribution of the ratio of excess temperature and $\mathrm{C}_{\mathrm{anth}}$. Generally, the intermediate value histogram (κ_i^T, magenta line) resembles the final ratio (κ_r^T, blue line), with the exception of the large peak at zero, resulting from the suppression factor, ϕ_T. The positive tail of κ_r^T values is predominantly due to the inversion of the DIC field with depth in the North Pacific. That the correlation between the redistribution of temperature and carbon is positive here implies that the method of Williams et al. (2021) may not be appropriate in this location. However, the shape of our distributions are in clear agreement with their method: our decomposition infers negative correlations between redistributed temperature and natural carbon, and positive correlations between excess temperature and anthropogenic carbon, in general. As our method identifies correlations between excess temperature and anthropogenic carbon, and between redistributed temperature and natural carbon changes that are consistent with both the assumptions of Williams et al. (2021) and Bronselaer and Zanna (2020), despite not enforcing this to be the case, we have confidence that it is reliably separating excess and redistributed temperature.

We now compare estimates of excess temperature from our method and that of Bronselaer and Zanna (2020): both methods producing consistent estimates indicates we are accurately identifying the excess temperature field. Figure 2 shows the zonally averaged excess and total temperature fields we obtain for the Atlantic and Indo-Pacific, for the final decade of our simulations, 2090-2099. In the Atlantic and Indo-Pacific, the estimate using the method of Bronselaer and Zanna (2020) (2a,b) produces smoother estimates than our technique (2c,d), but there are a number of common features which both techniques identify that are not due to the accumulation of excess heat. In the Atlantic, the tongue of warming at 2000-2500m depth, extending from approximately 40°N to 30°S is identified by both techniques as redistribution of the preindustrial temperature field, rather than excess heat. In addition, both techniques identify the region of warming extending from approximately 2000-4000m depth between 60°S and 40°S as redistribution, rather than excess heat. In the Indo-Pacific, both methods identify the cooling at approximately 1000m at 20°S as redistribution, rather than excess temperature. However, our method identifies the penetration of excess temperature to depth in the Southern Ocean, unlike the method of Bronselaer and Zanna (2020).

In the upper 1000m, there are significant divergences between the two techniques. To explore the sources of these differences, we compute local estimates of the quantity $\Delta\Theta_e/\Delta\mathrm{C}_{\mathrm{anth}}$ from our estimates of $\Delta\Theta_e$ and model $\mathrm{C}_{\mathrm{anth}}$. By comparing our locally obtained estimates with the patterns of excess heat and anthropogenic carbon uptake estimated by assuming a globally uniform α_T, we are able to show how our relaxation of the assumption of a globally uniform α_T causes our estimates to differ. This is demonstrated in Figure 3.

Figure 3a and 3b show local values $\Delta\Theta_e/\Delta\mathrm{C}_{\mathrm{anth}}$, presented as the zonal mean of the ratio of total excess temperature accumulated to total anthropogenic carbon accumulated, averaged over the decade 2090-2099. Figure 3c and 3d show the differences between the excess temperature estimated using our technique, and estimated using the technique of Bronselaer and Zanna (2020), and Figure 3e, 3f shows the total $\mathrm{C}_{\mathrm{anth}}$ accumulated over the same period and domain.

At depths of below 2000m in the Atlantic and 1000m in the North Pacific, ventilation is negligible and so despite large $\Delta\Theta_e/\Delta\mathrm{C}_{\mathrm{anth}}$ estimates, the two methods produce similar estimates of excess temperature. In the Southern Ocean, North Atlantic and North Pacific, we see large $\Delta\Theta_e/\Delta\mathrm{C}_{\mathrm{anth}}$ values, as well as nontrivial accumulation of excess temperature. We therefore find that in these regions, our estimates of excess temperature and those using the method of Bronselaer and Zanna (2020) diverge.

In general, our estimates of $\Delta\Theta_e/\Delta\mathrm{C}_{\mathrm{anth}}$ show a large degree of spatial coherence, despite no constraints being imposed to enforce this. This gives us confidence that these variations are likely real, rather than an artifact of our estimation technique. An implication of this is that heat uptake is intensified, relative to $\mathrm{C}_{\mathrm{anth}}$ uptake, in the high latitude Northern Hemisphere, and

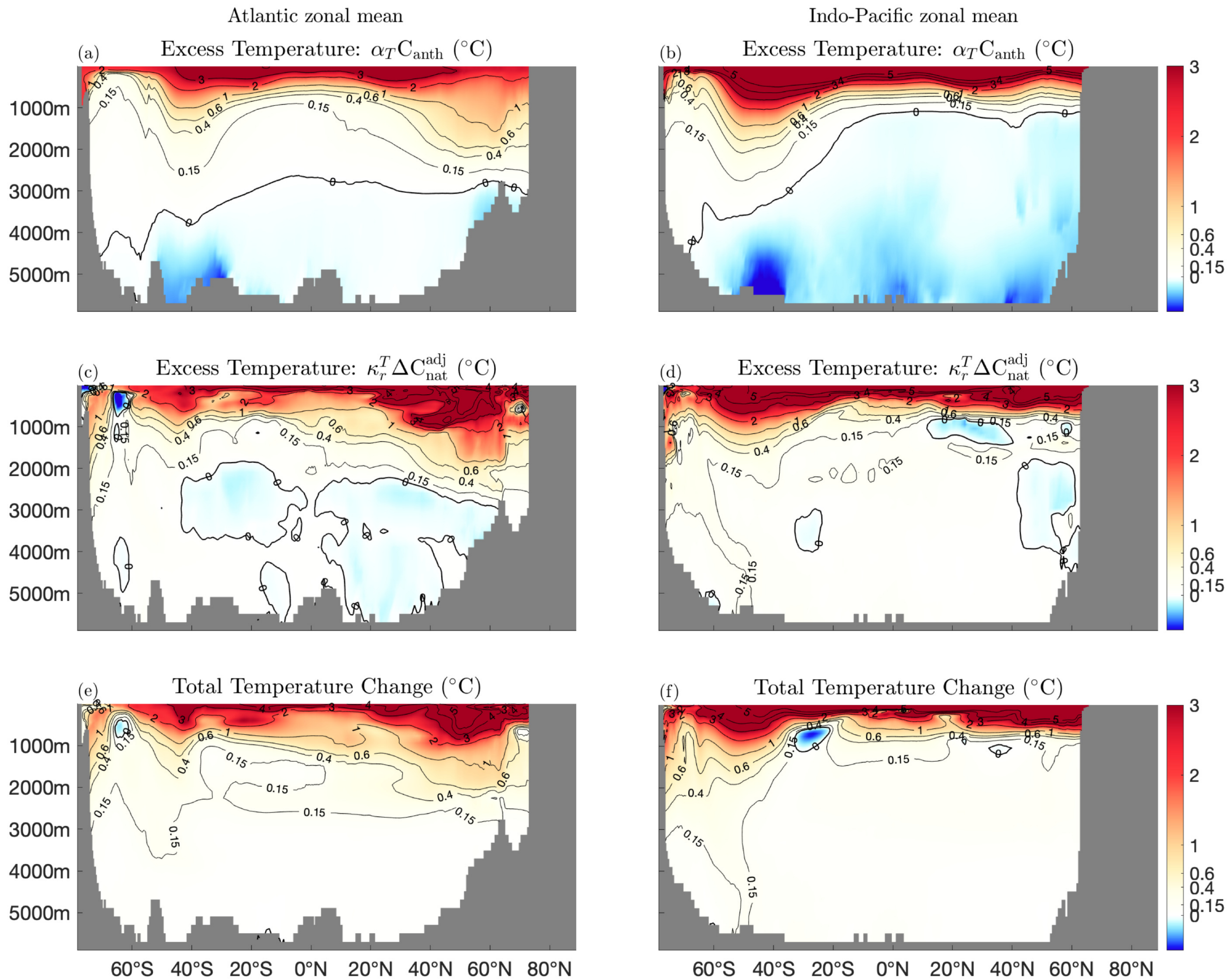

Figure 2. Atlantic and Indo-Pacific zonal, decadal mean excess temperature estimates, for the decade 2090-99, and total temperature change. The method of Bronselaer and Zanna (2020) is shown in panels (a,b), our method in panels (c,d), and the total temperature change in panels (e,f). The thick black contour indicates the zero contour, and temperature changes are indicated by thin contours, which are also indicated on the colour axes.

reduced in the low latitude Northern Hemisphere and Southern Hemisphere. We suggest that this may be explained in terms of a reduction of carbon export through the mixed layer at high latitudes. Bronselaer and Zanna (2020) make an argument for a globally uniform α value based on surface carbonate chemistry. However, Bopp et al. (2015) found total $\mathrm{C_{anth}}$ subduction through the base of the mixed layer to be significantly more variable than air-sea $\mathrm{C_{anth}}$ fluxes, and generally reduced at high latitudes (their Figure 3c): this mechanism could potentially act to reduce the spatial uniformity of α below the base of the mixed layer. In particular, water masses where the effects of advection and vertical mixing on carbon subduction are in opposition (namely high latitudes) tend to produce higher values of $\Delta\Theta_e/\Delta\mathrm{C_{anth}}$.

To test whether these variations in local values of $\Delta\Theta_e/\Delta\mathrm{C_{anth}}$ may constitute a source of error in the method of Bronselaer and Zanna (2020), we also compare the column inventories of excess heat uptake over the top 2000m of the ocean obtained using both methods in our simulations: this is shown in Figure 4. Bronselaer and Zanna (2020) were able to directly compare their estimates of excess heat and the simulated excess heat (their Figure 3f). We find that though our estimates do differ, these differences (Figure 4c) closely resemble those between their method and the simulated excess (their 3f). The zonally integrated difference in upper 2000m excess heat content (Figure 4d) is again consistent with a reduction of carbon export through the mixed layer base at high latitudes.

As our method produces results broadly consistent with both the method of Bronselaer and Zanna (2020) and Williams et al. (2021), we believe it is reliably identifying excess temperature. In addition we find a plausible explanation for differences between the results of the two methods, that is consistent with the inference that the spatial variability in the ratio of $\mathrm{C_{anth}}$ and excess heat accumulation is realistic.

3.2 Inventory Changes

Global mean excess and redistributed salinity change, as well as globally integrated excess and redistributed heat content change are shown in Figure 5. The global mean excess and redistributed salinity (thick lines, Figure 5a) begin to decrease in 1891, when the RAD and CTR forcing ceases to be identical, though this sea ice melt driven decrease is much smaller than the scale of either the positive and negative only excess or redistributed salinity components (thin dashed lines): global mean excess and redistributed salinity both decrease by approximately 0.001PSU over the full run. Globally integrated excess heat does not begin to accumulate significantly until approximately 2000: until this point, both positive only (global integral of excess heat content only in regions where excess temperature is positive) and negative only excess and redistributed heat are of similar scales. Positive only excess heat and globally integrated excess heat are approximately the same by 2050, and negative only excess heat increases from approximately -200ZJ in 2000 to approximately -50ZJ by 2100: some negative excess heat due to cooling in the first half of the run remains throughout the full simulation.

The global integral of positive and negative only regions are useful for assessing the extent of redistribution: whilst the global integral of redistributed temperature is constrained to be zero, this is the result of the cancellation of the positive and negative regions. Whilst excess heat begins to dominate during the mid 21$^{\mathrm{st}}$ century, the extent of temperature (and salinity) redistribution continually increases: there is no indication of ‘settling’ into a new circulation state, where redistribution ceases to increase, on the timescale of the full simulation. This can be seen from the continued and accelerating increases in positive

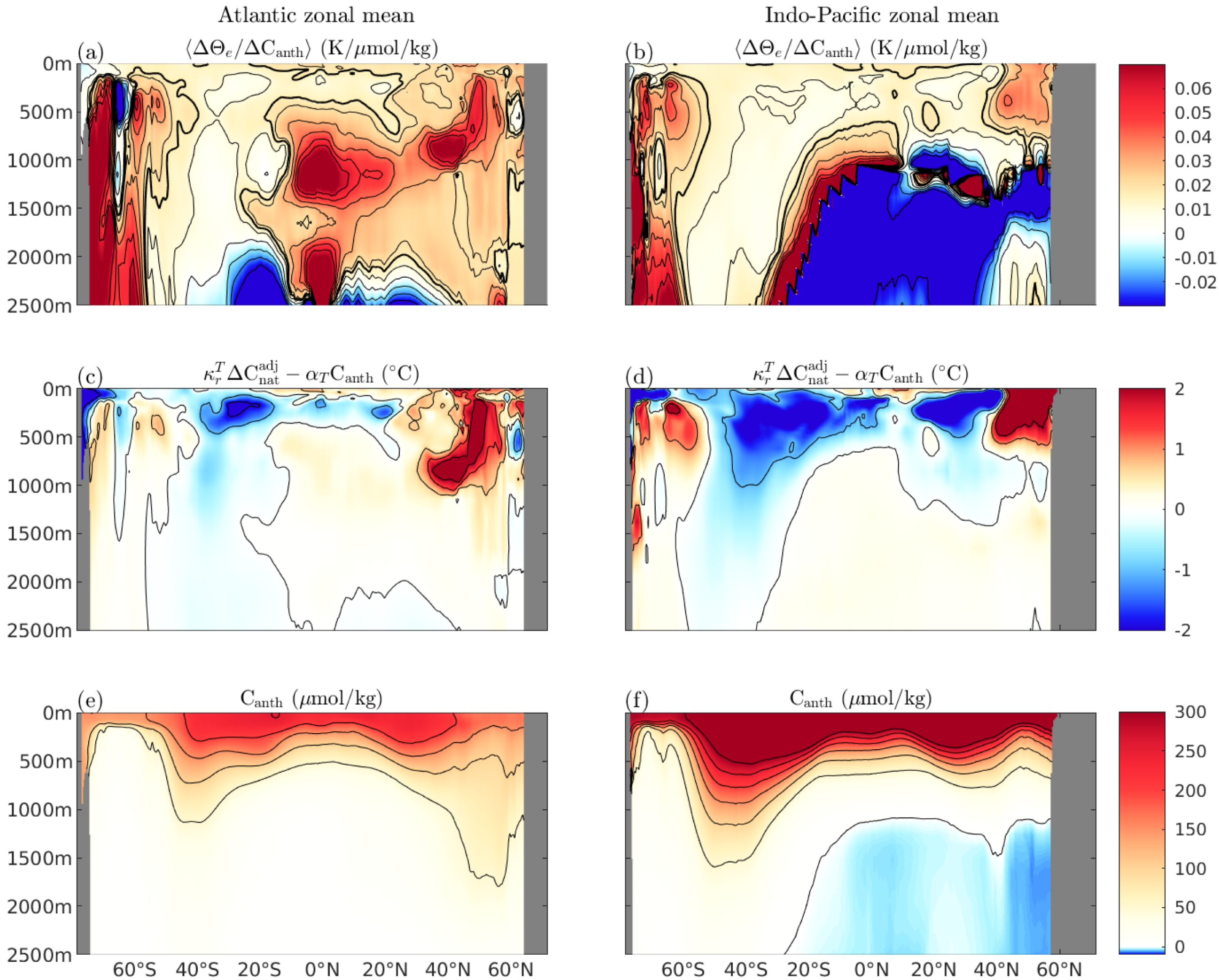

Figure 3. Atlantic and Indo-Pacific zonal mean ratio of excess temperature to C_{anth} accumulation, calculated as the 2090's decadal, zonal mean temperature divided by 2090's decadal, zonal mean C_{anth} (Panels (a), (b)). Panels (c) and (d) show the difference between our excess temperature estimate and the excess temperature estimate produced using the method of Bronselaer and Zanna (2020), and Panels (e) and (f) the zonal mean C_{anth} accumulation, calculated as the 2090's decadal mean. The thick black contour in Panels (a), (b) indicate the global mean value of α_T of 0.016K/μmol/kg, and the thin contours are indicated on the colour axes.

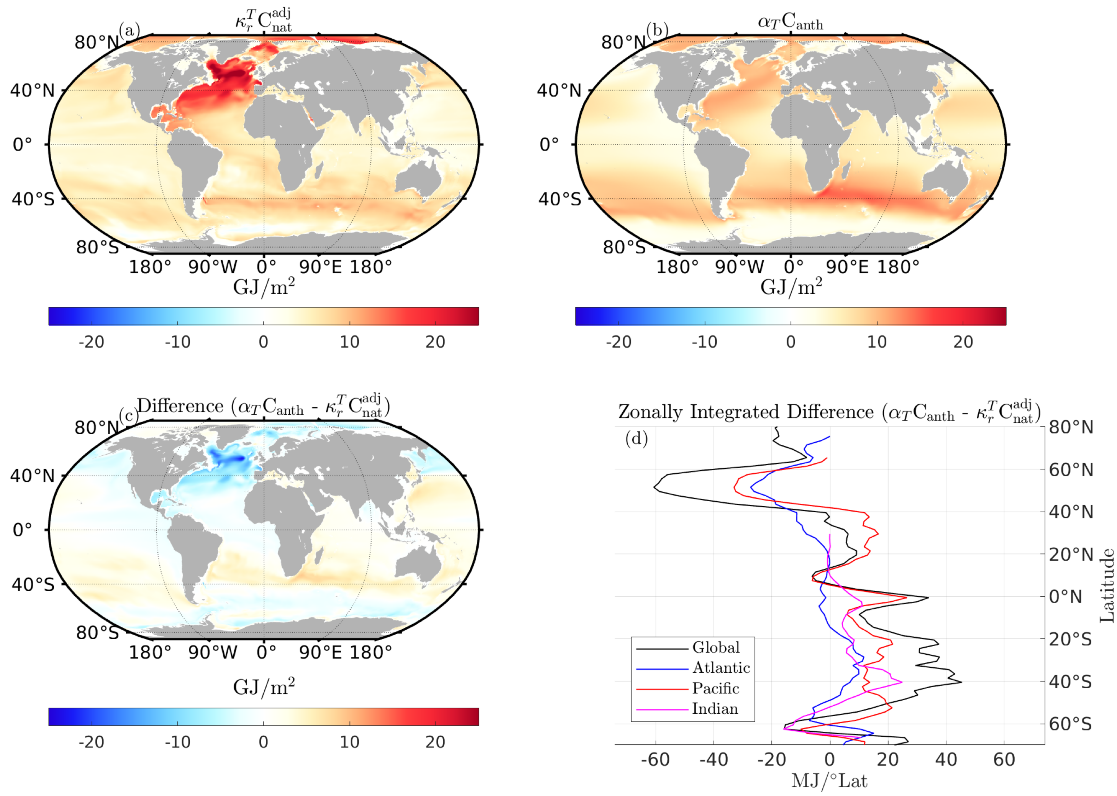

Figure 4. Column inventories of excess heat (0-2000m), calculated as the 2090-2099 decadal mean excess temperature relative to preindustrial. Panel (a) shows our method, panel (b) the method of Bronselaer and Zanna (2020), and panel (c) the difference between the two estimates. Panel (d) shows the zonally integrated upper 2000m excess heat content difference.

and negative only redistributed heat and salinity. We also observe that whilst the magnitude of positive and negative only redistributed heat are similar until approximately 2000, excess salinity is significantly larger than redistributed salinity at all times. This indicates that during the full course of our simulations, salinity changes are dominated by changes in the freshwater cycle, rather than changes in circulation.

For comparison, we include observational estimates of ocean heat uptake from Zanna et al. (2019) (Figure 5b): cumulative heat uptake over 1871-2015 in grey (436±91ZJ) and over 1995-2015 in green (153±44ZJ). Over the period 1871-2015, our simulations underestimate cumulative heat uptake (249ZJ), but overestimate heat uptake over 1992-2015 (232ZJ).

Figure 6 shows the integrated redistributed and excess temperature, salinity, and densities for each ocean basin. As with the global mean, excess salinity begins to accumulate almost immediately in most ocean basins (Figure 6c), particularly the North Atlantic and South Pacific: trends here are distinct from noise at 2σ in 1893 and 1911, respectively. Excess temperature does not begin to accumulate until the 21$^{\mathrm{st}}$ century, at which point it begins to rapidly accumulate in all ocean basins; the exception to this is the South Atlantic (Figure 2a, dashed black line) which cools in the 20$^{\mathrm{th}}$ century, its excess heat signal emerging from

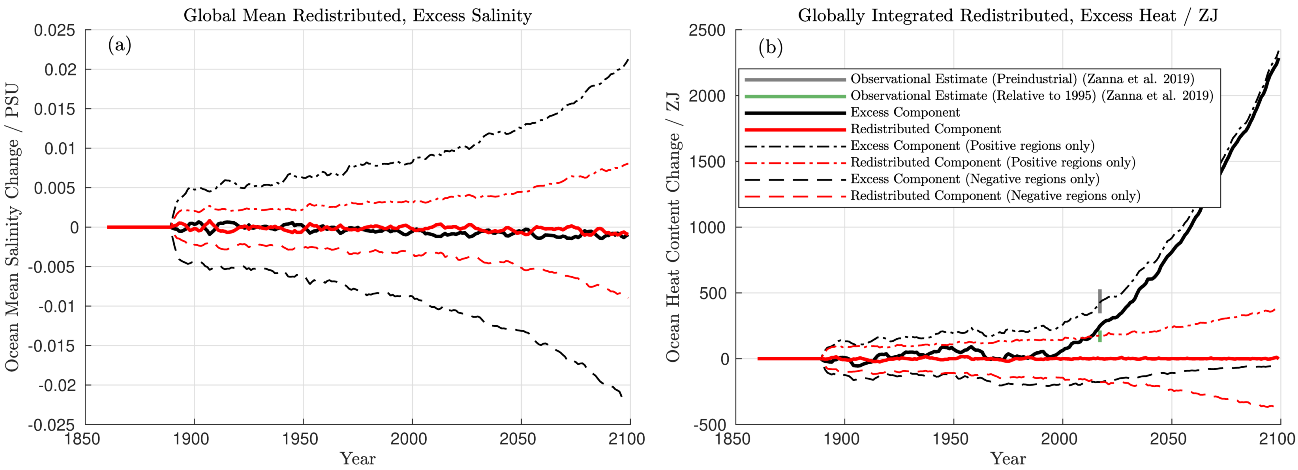

Figure 5. Global mean excess and redistributed salinity (a), and globally integrated excess and redistributed heat (b). Excess components are shown in black, redistributed components in red. The integrals of only the positive and negative regions are also shown (thin dashed lines). Climate change and control runs use the same first 30 years of forcing, so values are by definition zero here: the jump in 1890 represents the initial divergence of states. Observational estimates of global ocean heat uptake from Zanna et al. (2019) are also shown in panel (b).

noise at 2σ in 1918. In contrast, the excess heat signal in the North Atlantic and South Pacific do not emerge from noise at 2σ until 2023 and 2021, respectively. Over the period 2023-2099, for which the excess heat signal of the North Atlantic is distinct from noise, $25{\pm}2\%$ of global excess heat accumulated is located in the North Atlantic.

The accumulation of negative excess density is dominated by the accumulation of excess temperature, rather than salinity: the grey scales on the right hand side of panels (a)-(d) show the density change associated with heat and salinity change. In the North Atlantic, changes in the excess heat and salinity compensate to reduce density anomalies: a reduction of almost 25Pg associated with excess heat is compensated for by an increase of approximately 8Pg associated with increased salinity. Similar compensation, though much weaker, is seen in the South Atlantic, which cools and freshens during the 20^{th} century before warming and salinifying in the 21^{st}. This is not the case in other basins, where the changes in excess heat and salinity both act to decrease density and therefore increase stratification.

The redistribution of density is less dominated by heat, with heat and salinity contributing similarly to redistributed density. In the North Atlantic, the redistribution of heat and salinity are approximately density compensated until around 2050, at which point the redistributed density inventory begins to increase rapidly (Figure 6f, black line). Good density compensation in the redistributed component is also seen in the subantarctic Southern Ocean, with minimal accumulation of redistributed density.

In our COU run, AMOC strength (calculated as peak depth integrated meridional volume transport at 26°N) increases until 1990 before declining continually thereafter. The cumulative transport anomaly (time integrated difference between COU and CTR AMOC volume transport) peaks in 2035 before also declining continually for the rest of the simulation. The signal of AMOC decline is visible in the redistributed heat content of the North Atlantic, which peaks in 2037 before declining rapidly,

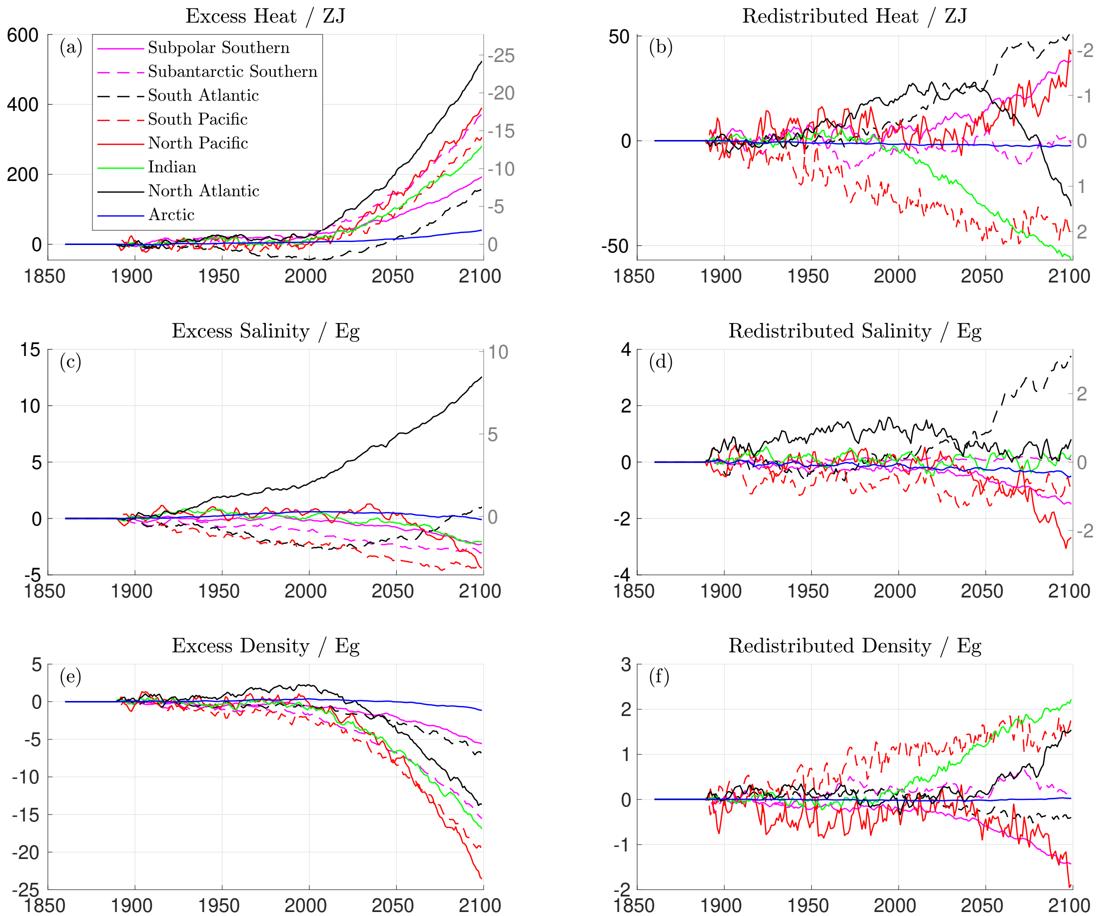

Figure 6. Excess (left column) and redistributed (right) heat, salinity and density integrals for each ocean basin over the full model run. For the changes in heat and salinity (Panels (a)-(d)), the equivalent integrated density change in units of Pg are given in grey on the right. Scales differ for excess and redistributed components, and changes in salinity and density are given as mass changes rather than volumes.

as well as the redistributed salinity content of the South Atlantic, which begins to increase at approximately the same time: consistent with previous studies (Zhu and Liu, 2020) which find a 'pile up' of salinity in the South Atlantic as a result of AMOC slowdown. The AMOC in our simulations is too weak, with a preindustrial mean of approximately 7.5Sv at 26°N, and a maximum value of 13Sv in our COU run, declining to approximately 4.5Sv by 2099, as compared to approximately 15Sv in HadGEM2-ES (Martin et al., 2011) and 18±4.9Sv observationally (Johns et al., 2011). This AMOC strength at 26°N in HadGEM2-ES itself is towards the weaker end of estimates from CMIP5 models (Weaver et al., 2012). However, the heat transport is realistic, with a control run heat transport of 0.075PW/Sv at 26°N, as compared to observations of 0.079PW/Sv

(Johns et al., 2011). The decline in AMOC strength in our ocean only simulations and HadGEM2-ES simulations are also proportional: over an RCP8.5 scenario, Sgubin et al. (2014) found a decline of AMOC strength at 26N from approximately 15.5 to 8Sv at 26°N in HadGEM2-Es.

To explicitly test whether the redistribution of heat from the North Atlantic, and salinity to the South Atlantic, can be explained in terms of a changing AMOC, we calculate the redistribution of heat and salinity through the Equator in the Atlantic. This is calculated as the difference in meridional velocities between the COU and CTR runs, multiplied by the control run temperature and salinity fields (this analysis is conceptually similar to that performed by Williams et al. (2021) in order to calculate the redistribution into/out of a volume, though here we consider only the equatorial boundary between the North and South Atlantic). For the period 1950-2099, for which there are non negligible changes in the redistributed heat content of the North Atlantic, we find the correlation between the redistributed heat content of the North Atlantic and the redistribution of heat through the Equator due to AMOC change has an R^2 value of 0.58, suggesting that the changing in overturning circulation plays a key role redistributing heat out of the North Atlantic, and into the South Atlantic. We also find a slightly weaker correlation between the non AMOC driven redistribution of heat past the equator and the North Atlantic heat inventory, with a R^2 value of 0.45. These R^2 values are reduced to 0.50 and 0.38, respectively, when considering the period 1890-2099.

The picture is similar for salinity: for the period 2000-2099, for which there are non negligible changes in the redistributed salinity content of the South Atlantic, we find a correlation between the redistributed salinity content of the South Atlantic and redistribution of salinity through the equator due to AMOC change has an R^2 value of 0.61, which is reduced to 0.04 when considering the period 1890-2099. Changes due to gyre circulation driven redistribution have R^2 values of 0.09 and 0.33, respectively, suggesting that the large scale mechanisms of salinity redistribution differ from those of heat.

As this method of calculation is able to infer redistribution directly from model outputs, we have good confidence our decomposition is reliably identifying excess heat and salinity. We therefore believe the redistribution of heat out of the North Atlantic and salinity into the South Atlantic are driven predominantly by AMOC variability, with non AMOC circulation changes influencing the redistribution of temperature and salinity differently. Identifying whether the lack of correlation between our estimates and the explicitly calculated redistribution when there is no appreciable accumulation of either is due to inaccuracies in our approach or the dominance of other factors in the redistribution of heat and salinity would likely improve our understanding of the strengths and weaknesses of this method, but is beyond the scope of this study.

As with the global inventories, we find little evidence of ‘settling’ into a new circulation state: in most basins, redistributed heat and salinity inventories do not cease to grow during our simulations, and AMOC strength declines continually throughout the 21st century. A notable exception is the South Pacific, for which the redistributed heat inventory increases to approximately -50ZJ by 2050, before remaining at a similar value for the rest of the simulation.

One way of assessing the interaction of excess and redistributed heat is to plot changes in their accumulation against each other, with emergent relationships consistent with coupling between the two: this is shown in Figure 7.

In the North Atlantic, we find an acceleration of the accumulation of redistributed heat with respect to the excess heat inventory (Figure 7g). However, in all other basins for which relationships emerge clearly, the accumulation of excess and redistributed heat are either linearly related (Subpolar Southern (7a), North Pacific (7e)), or sublinear. This is as expected: the

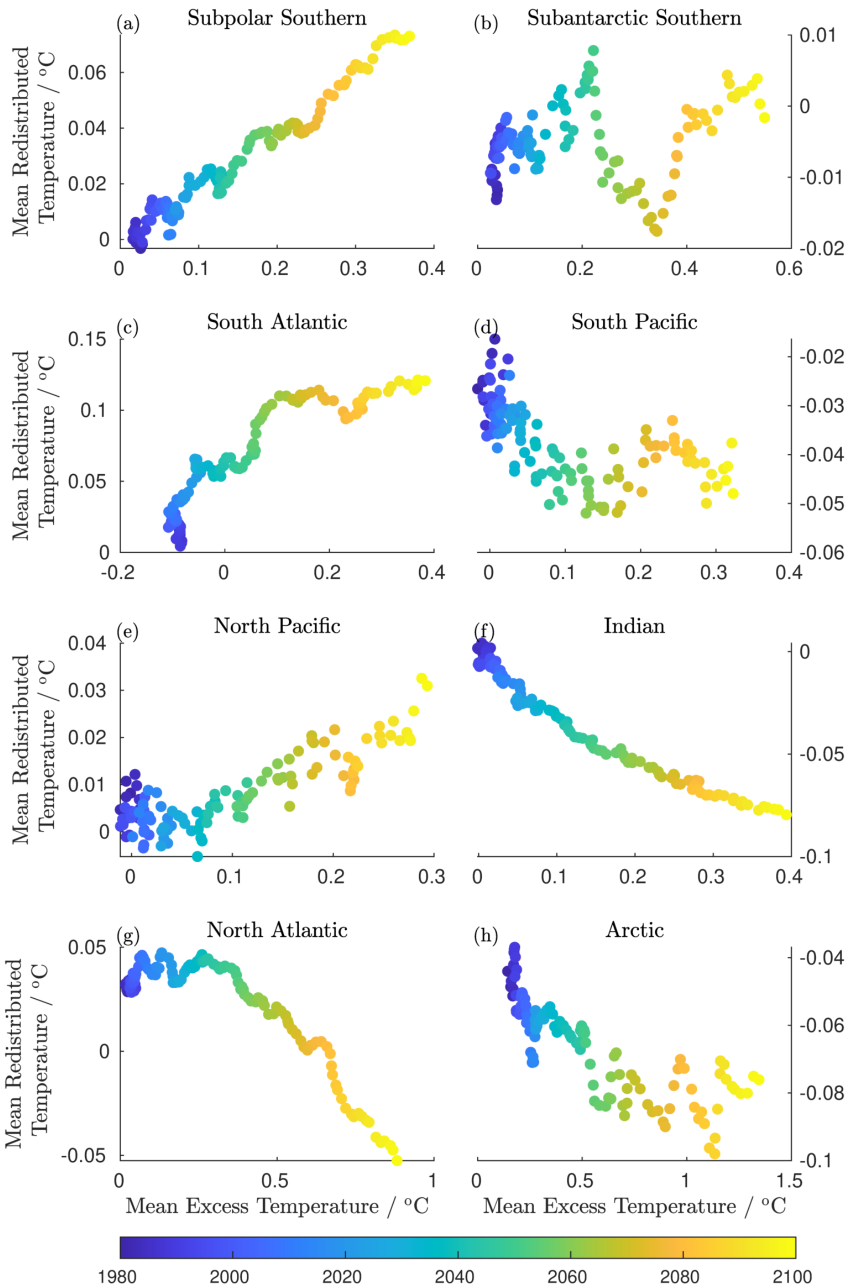

Figure 7. The emergent relationships (if any) observed between excess and redistributed heat in each of the 8 ocean basins shown in Figure 7, presented in terms of the mean redistributed and excess temperature changes for the basin. Timeseries begin in 1980 as there is no appreciable accumulation of excess or redistributed heat in the first half of the run. Scales differ for each basin.

acceleration of the accumulation of redistributed heat is unique to the North Atlantic. In all basins other than the North Atlantic, the rate of accumulation of redistributed heat with respect to excess heat slows over the timeseries.

Despite this slowing, the redistributed heat inventories continue to grow, except in the Subantarctic Southern, South Atlantic, South Pacific and Arctic. In all other basins, we see the continued accumulation of redistributed temperature, indicating the continual dynamic readjustment of the ocean, at an inter-basin scale: the lack of growth at a basin scale imposes no constraints on intra-basin redistribution. Of these, the Subpolar Southern and North Atlantic are the most striking, with heat redistribution increasing linearly and with the square of excess heat accumulation, respectively.

Previous studies have found AMOC strength to be proportional to SST anomalies in the North Atlantic (Caesar et al., 2018), and SST anomalies are thought to be proportional to excess heat (MacDougall and Friedlingstein, 2015). Though it would initially appear that this would act to linearly couple the excess heat content of the North Atlantic to the redistribution of heat out of the North Atlantic, the redistributed heat inventory will be proportional to the time integrated changes in AMOC strength. The excess heat inventory of the North Atlantic increases monotonically with time, and so the rate of change of the redistributed heat inventory will be proportional to the excess heat inventory. The proportionality of the redistributed heat inventory of the North Atlantic to the excess heat inventory can therefore be explained in terms of the unique circulation of the North Atlantic.

3.3 Mapping storage of excess and redistributed temperature and salinity

The regional patterns of decadal mean excess and redistributed temperature for the 2090s at the surface and at 2000m is shown in Figure 8 and the regional patterns of the 2090s decadal mean excess and redistributed salinity in Figure 9. For both temperature and salinity, surface changes are dominated in most locations by the excess component. Excess temperatures are positive nearly everywhere, whilst excess salinity is generally positive in the South Atlantic, Subtropical North Atlantic and Indian Oceans, with the Pacific generally negative. This is consistent with increased evaporation over the Atlantic and increased atmospheric freshwater transport from the Atlantic to the Pacific.

It is generally expected that in a warming climate, the hydrological cycle will become amplified, with increased evaporation (precipitation) in regions of net evaporation (precipitation) (Durack and Wijffels, 2010), (Zika et al., 2018), (Gould and Cunningham, 2021). Thus, salty regions of the ocean surface become saltier, and fresh regions fresher. As these changes result from changing surface fluxes, hydrological amplification should be captured by the excess salinity at the surface, rather than redistributed salinity: this is consistent with our results.

Whilst surface warming is unsurprisingly dominated by excess temperature, at 2000m the contributions of excess and redistributed temperature to total temperature change are of comparable magnitude, with the exception of the North Atlantic. In contrast, the majority of salinity change at depth is accounted for by the excess component, though appreciable changes are generally only found in the North Atlantic. This salinity increase at depth is despite surface freshening in the Subpolar North Atlantic (Figure 9a, 9c), resulting from the propagation of surface salinification here in the 20$^{\text{th}}$ century. Patterns of excess and redistributed surface salinity are consistent with the results of Sathyanarayanan et al. (2021) and Levang and Schmitt (2015).

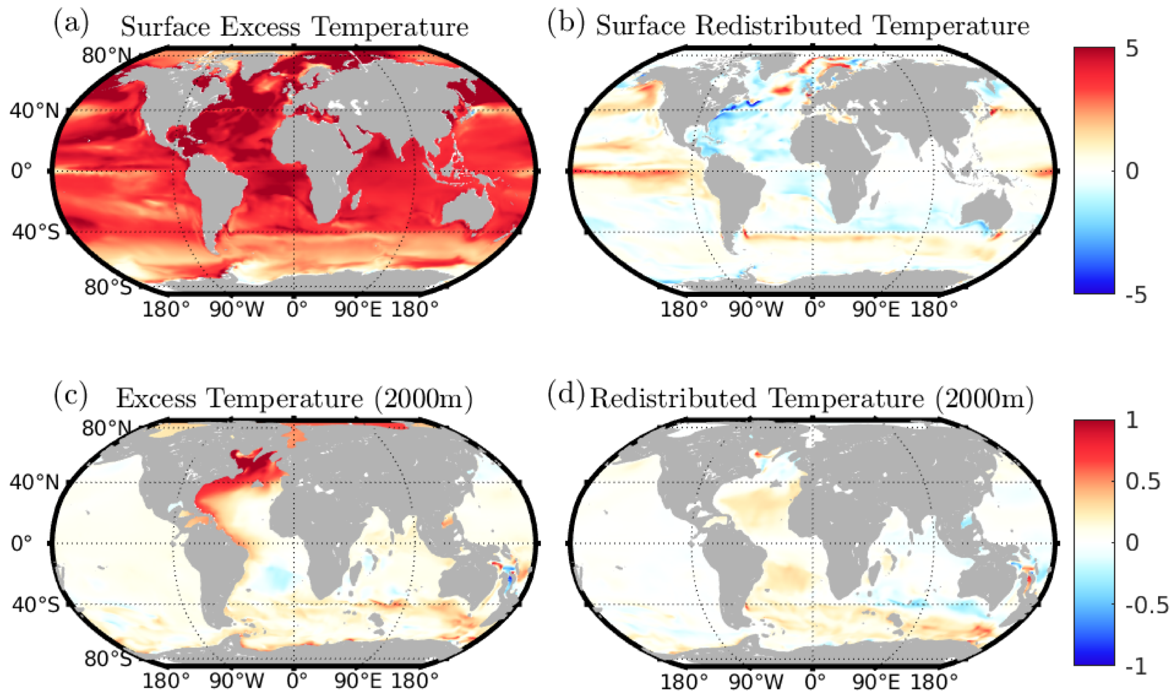

Figure 8. Maps of excess and redistributed temperature on two depth surfaces: the surface and at 2000m. Values given are the decadal mean for the decade 2090-2099. Colour axes are shared between each component at both depths.

The strong surface redistributed salinity signal in the Arctic appears to result from reduced sea ice freshwater transport from the marginal seas of the Arctic inwards. Previous studies using the NEMO GCM coupled to the LIM2 sea ice model have found that Arctic sea ice tends to grow along the coastal shelves of the Arctic Ocean, before being transported by the Beaufort Gyre circulation and transpolar drift (Moreau et al., 2016). The net result of this is to transport both freshwater and DIC from the coastal shelves to the centre of the Arctic Ocean: changes in this transport will therefore act to cause large and tightly correlated changes in DIC and salinity in the surface Arctic Ocean. Our decomposition therefore partitions salinity change resulting from changes in this transport to redistribution. Similar changes in sea ice transport also act to cause redistributed freshening in the coastal Southern Ocean.

The total inventory change in heat, salt, and density by the last decade of our simulation, as well as the storage of the excess and redistributed components are shown in Figure 10, for the upper 2000m of the ocean. We present these as contributions to steric sea level change, allowing for both normalisation and a comparison of contributions to steric sea level rise. On this timescale, excess (Figure 10c) and total (Figure 10a) heat inventory changes are positive nearly everywhere, with the exception of the Weddell and Ross Gyres. Redistributed heat inventories are negative generally in the North Atlantic (Figure 10c), with the largest values seen in the Labrador and Norwegian Seas, as well as the Subtropical Gyre. In the Pacific and Indian Oceans, redistributed heat inventories are most negative at around 30-35°S.

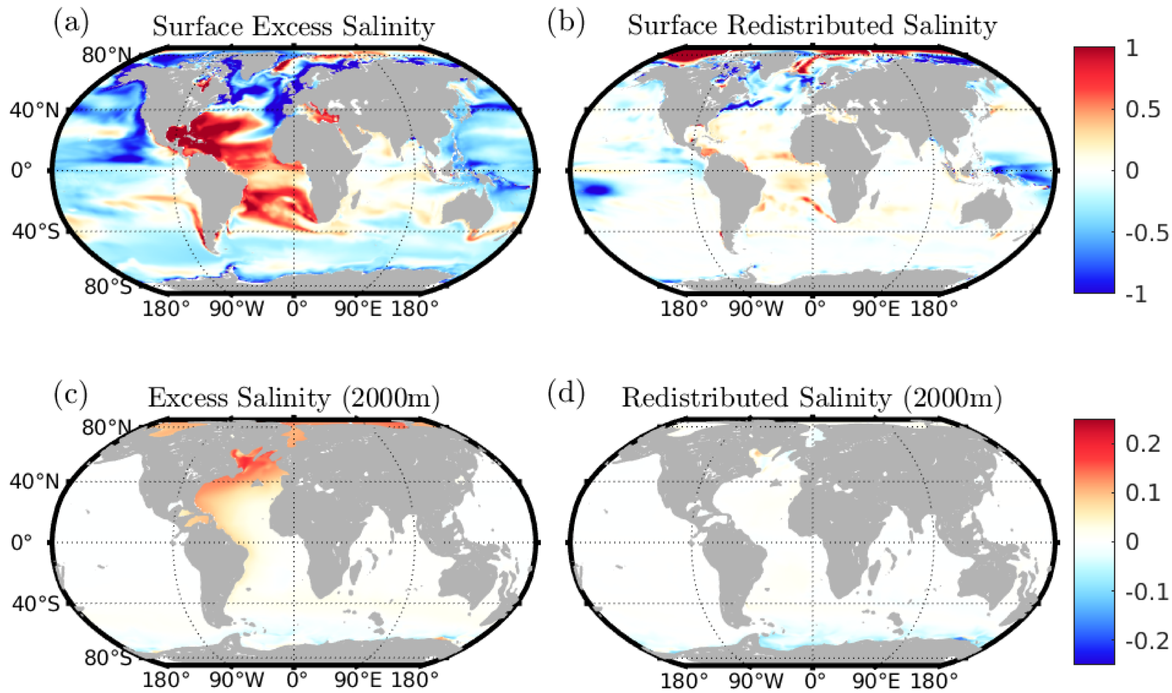

Figure 9. Maps of excess and redistributed salinity on two depth surfaces: the surface and at 2000m. Values given are the decadal mean for the decade 2090-2099. Colour axes are shared between each component at both depths.

Salinity inventory changes show a different geographical distribution: excess salinity increases uniformly only in the Atlantic and Arctic oceans (Figure 10e). Total salinity change is again dominated by the excess here. As with heat, the fingerprint of AMOC slowdown can be seen in the redistributed salinity signal: we observe redistribution driven cooling and freshening in the North Atlantic and redistribution driven warming and salinification in the Equatorial and South Atlantic, resulting from a weakening in the northward transport of heat and southward transport of fresh water. This redistribution driven cooling and freshening acts to oppose the warming and salinification associated with increased surface heating and concurrent increases in evaporation - precipitation (E-P).

Density inventory changes (Figure 10a) are relatively globally uniform compared to the individual contributions: a decrease is seen in the total change and excess inventory nearly everywhere, with the exception of the Weddell and Ross Seas, as well as the central Arctic Ocean. The Arctic Ocean decrease is dominated by the changes in freshwater transport, whereas the Weddell and Ross Sea decrease result from upwelling cool water. In the Atlantic, large changes in steric sea level resulting from excess temperature are significantly reduced by the accumulation of excess salinity, and a similar cancellation is seen in the redistributed components.

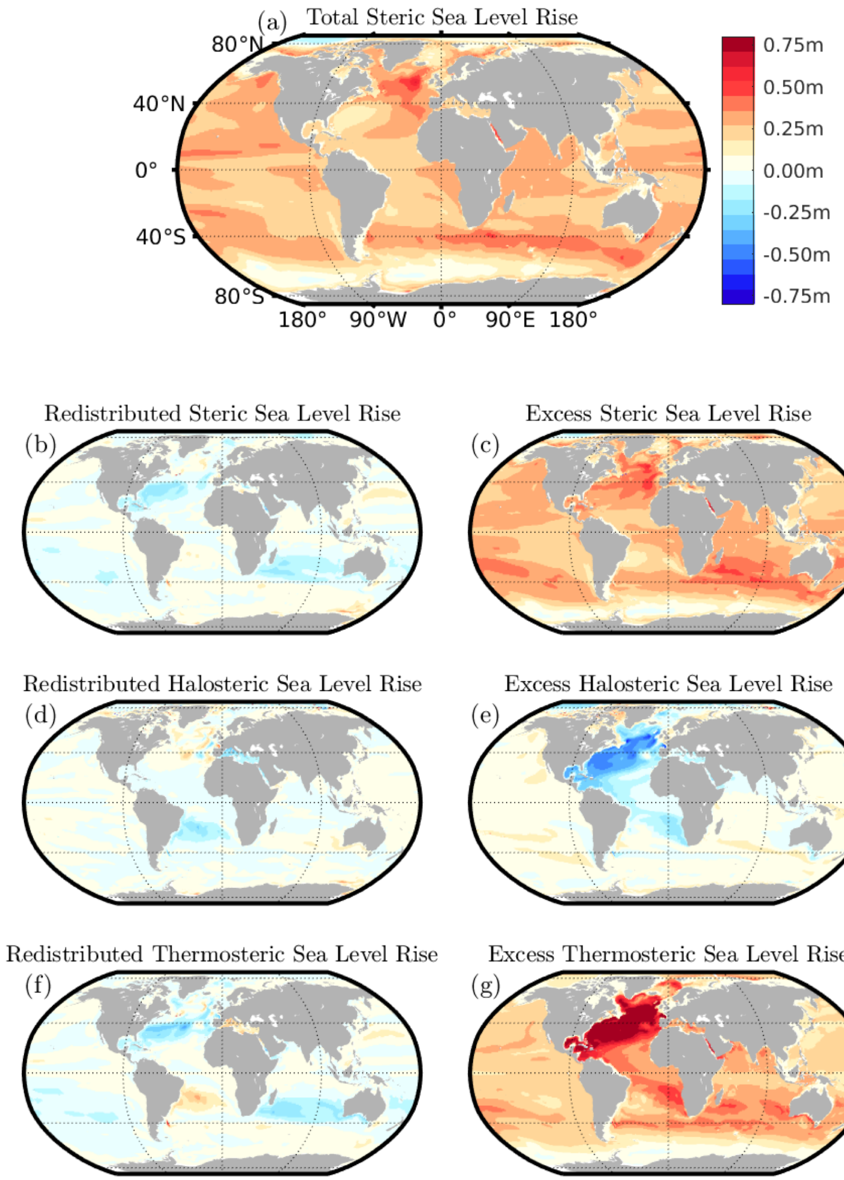

Figure 10. 2090's mean steric, halosteric and thermosteric contributions to sea level rise, as well as the total, from the upper 2000m of the ocean.

4 Discussion and Conclusions

We have demonstrated a new technique for estimating the redistribution of heat and salinity by the ocean in response to anthropogenic climate change, allowing us to identify the excess signal and producing estimates consistent with other reconstructions. This method can be thought of as sitting within a family of techniques which aim to understand ocean circulation changes through the relationship between ocean temperature and DIC, along with the methods of Bronselaer and Zanna (2020) and Williams et al. (2021). It produces results which are consistent with the assumptions of both methods, without constraints to enforce this. Instead, we assume that on decadal and subdecadal timescales, local ocean heat and carbon content are dominated by redistribution, and that on longer (multidecadal to centennial) timescales, circulation variability dominates over biological changes in natural carbon. This first assumption is consistent with the results of Thomas et al. (2018), who investigated the relationship between ocean heat and carbon content, finding the two to be anticorrelated on decadal timescales. The results of Williams et al. (2021) suggest the assumption of circulation variability dominating over biologically driven changes is also reasonable. A key strength of this new technique is that it also allows us to estimate not only the redistribution of heat, but also salinity, and in principle can be extended to other tracers whose distributions that evolve in response to anthropogenic climate change. Furthermore, its implementation is such that in order to identify circulation driven changes in a given tracer requires only timeseries of the tracer in question, and a tracer which we may assume to change distribution only through redistribution, for example $\mathrm{C_{nat}}$. It should therefore also be applicable to observational timeseries with little modification.

Our globally integrated estimates indicate that the excess and redistributed temperature signals are currently of a similar size, with excess temperature signals expected to exceed the redistributed temperature signals towards the end of the 2020's. This is in keeping with previous studies which find excess heat beginning to dominate over redistributed heat in the period 2011-2060 (Bronselaer and Zanna, 2020). Of course, as this is only one climate change run from a single model, there is a large uncertainty associated with this and we recognise that it does not account for the spread of model responses to imposed climate change under an RCP8.5 scenario. However, our results are internally consistent, demonstrating a number of phenomena thought to occur under a changing climate explicitly in terms of the accumulation of excess heat and redistribution of preindustrial heat.

We have also produced, to our knowledge, the first modelled estimates of the redistribution of the preindustrial salinity field by the ocean and so the excess salinity field: that is, the changes in salinity due to changes in the balance of surface freshwater transport, directly excluding changes in ocean freshwater transport. By extension, we have also been able to produce estimates of excess and redistributed density, and so the contributions to steric sea level rise of temperature and salinity changes. We find that the penetration to depth of the redistributed salinity signal is far weaker than that of temperature, which, with the exception of the North Atlantic, accounts for a similar fraction of deep temperature change as the excess. However, we do find several signals in surface excess and redistributed salinity changes consistent with hydrological amplification, as well as a salinity signal in the South Atlantic as a previously identified 'salinity pile up' in the South Atlantic consistent with AMOC slowdown (Zhu and Liu, 2020). By the 2090's, the Southern and Subtropical North Atlantic show increasing redistributed surface salinity as a result of AMOC slowdown, with a decreasing redistributed salinity in the Subpolar North Atlantic. At the surface, we find that the majority of salinity change results from changes in E-P (excess), rather than circulation changes (redistributed), and that these patterns in excess salinity are consistent with both historical observations globally (Durack and Wijffels, 2010), and, in the Atlantic, with the salinity response to an idealised surface heat flux (Zika et al., 2018). We find that the decrease in global mean excess salinity occurs earlier than the increase in globally integrated excess heat, consistent with previous studies which find significant sea ice loss even in the early 20$^{\text{th}}$ century, before appreciable global warming (Wadhams and Munk, 2004), (Hetzinger et al., 2019). These results suggest that historical observations of temperature changes are dominated by redistribution, with excess temperature likely to dominate in the coming decades. Historical changes in salinity however may instead be predominately the result of excess salinity, rather than redistribution. This holds at both global and local scales, with the patterns of local excess salinity appearing to be dominated by amplification of the hydrological cycle, and is in agreement with the findings of Stott et al. (2008), Terray et al. (2012), Pierce et al. (2012) and Skliris et al. (2014), who suggest the salinification of the subtropical North Atlantic and freshening of the Western Pacific Warm Pool may constitute an early fingerprint of anthropogenic forcings.

In applying our technique to the Atlantic, we have shown explicitly the redistribution of heat associated with changes to the overturning circulation, in addition to the aforementioned salinity signal. We also find fingerprints of AMOC change in both the redistributed temperature and salinity inventories of the North and South Atlantic: a large and rapid accumulation of negative redistributed heat in the North Atlantic over the period 2037-2099, as well as the accumulation of a large inventory of redistributed salinity in the South Atlantic over the same period. Over the period 2023-2099, for which the accumulation of excess heat in the North Atlantic is distinct from noise, we find 25$\pm$2% of global excess heat accumulation is in the North Atlantic. This is remarkably similar to observational estimates of anthropogenic carbon uptake (Sabine et al., 2004), again indicating the close relationship between excess heat and anthropogenic carbon.

Whilst by the end of the 21st century heat storage is dominated by excess heat, excess salinity estimates are largely uniform, and the contributions of redistributed and excess salinity to halosteric SLR are of similar scales in most locations (Figure 10). The only exception to this is a large increase in excess salinity in the Atlantic, This is despite patterns of regional change in sea surface salinity and salinity inventory changes being dominated by the excess component, both historically and by the end of the 21st century. Though changes in salinity under anthropogenic climate change are expected to be less drastic than temperature, decomposing salinity into excess and redistributed components is also crucial to understanding the response of the ocean to global warming, due to its role in thermohaline circulation.

By combining our estimates of excess temperature and salinity, we can directly compute the excess density change, and the redistribution of density. In the North Atlantic, we find warming and salinification in the excess components, and cooling and freshening in the redistributed components. In both cases, these changes are in a density compensating fashion. Previous studies have noted that whilst density compensated water mass changes may be a general property of the ocean, the behaviour is particularly marked in the Atlantic (Lowe and Gregory, 2006), as well as important for contemporary Atlantic deep ocean heat uptake (Mauritzen et al., 2012), though it is uncertain how this will evolve. Our results suggest that in the Atlantic, even by the last decade of our simulations, changes in excess temperature and salinity act in a density compensating fashion. A consequence of this is that changes in surface freshwater fluxes associated with climate change oppose the reduction of overturning circulation associated with increased surface warming, opposing the reduction in the North Atlantic's capacity to sequester excess heat. This suggests that the excess contribution to themosteric SLR in the Atlantic will continue to grow on centennial timescales, assuming continued CO_2 emissions, though the thermosteric SLR is greatly ameliorated by halosteric sea level fall. This is in agreement with historical observations (Antonov et al., 2002). However, the much smaller redistribution contribution to density indicates that changes to ocean circulation will have little effect on steric SLR in the North Atlantic by the end of the 21^{st} century, although redistributed density compensation in the North Atlantic begins to break down in approximately 2050, as the redistribution of heat out of the North Atlantic significantly exceeds that of salinity by this time.

Finally, although only being applied within a single model, our patterns of excess and redistributed heat storage are consistent with previous studies (Winton et al., 2013), (Bronselaer and Zanna, 2020), (Williams et al., 2021), despite differing assumptions used in the calculation of the redistribution of heat from carbon. A key benefit of the method introduced here compared to prior carbon based estimates of circulation change is that it is applicable both to observations and multiple tracers. In combination with other techniques, we believe this method to be a powerful tool for understanding causes of future ocean temperature, salinity and density change.

Code and data availability. The model output we use as well as the code used to decompose the temperature and salinity fields are available upon request. Core functionality for the decomposition is freely available at https://github.com/charles-turner-1/temp_decomp.

Appendix A: Uncertainty in estimates of local redistribution

We estimate a local gradient, $\Delta\Theta/\Delta\mathrm{C}_{\mathrm{nat}}$ or $\Delta S/\Delta\mathrm{C}_{\mathrm{nat}}$ by applying two dimensional PCA to the timeseries of yearly deviations of the two variables from their decadal mean values at each grid cell. This is equivalent to performing a total least squares fit to obtain a linear relationship between the two variables.

We then scale the data to normalise the ranges of Θ/S and $\mathrm{C}_{\mathrm{nat}}$ before again performing 2D PCA on our timeseries at each grid cell to estimate the fraction of the covariance contained within each principle component. This yields the fraction of the total variance explained by each principal component, which we refer to as ε_1 and ε_2: these can be thought of the axes of an ellipse describing a scatter cloud relating the two variables. A fit which is a perfect line can be thought of as the limit of this ellipse where $\varepsilon_1 \to 1$ and $\varepsilon_2 \to 0$. Conversely, an essentially random fit through a spherical cloud of points can be thought of as the case where $\varepsilon_1 = \varepsilon_2$.

We use the eccentricity of this ellipse as a suppression factor, ϕ_u:

$$\phi_u = \sqrt{1 - \left(\frac{\varepsilon_2}{\varepsilon_1}\right)^2} \tag{A1}$$

The need for conservative estimates of confidence in the fit is particularly important for fits in which no discernable correlation can be drawn: for these, gradients associating minor changes in $\mathrm{C}_{\mathrm{nat}}$ with large changes in Θ or S can be obtained, effectively at random, and so our suppression factor must remove these effectively. As we concern ourselves primarily with inventories, this approach was found to be preferable to including large uncertainties due to a small number of spurious points, or simply setting a threshold below which we do not attempt to diagnose the redistribution of heat. Only 6% of ε_1 values are scaled by a factor of $1/2$ or less: this was found to be a suitable compromise, with only the most unreliable estimates strongly suppressed.

Alternative methods may produce better quantifications of uncertainty, though are not considered here as the eccentricity method was sufficient for our purposes.

We then calculate the redistribution coefficient κ_r as

$$\kappa_r = \phi_u \times \kappa_s \tag{A2}$$

The implementation of this is demonstrated in Figure A1, for two points in the North Atlantic at approximately 24°N, 30°W and 850m and 1950m. The poorly correlated point, Figure A1a and A1c, is an extreme outlier, shown for demonstrative purposes. Here the fit is essentially random, and so estimates of temperature redistribution are scaled to reflect this uncertainty: the eccentricity of the ellipse described by the cloud of points in $\Theta - \mathrm{C_{nat}}$ space is used as a scale factor. For the strongly correlated point, shown in panels (b) and (d), temperature and $\mathrm{C_{nat}}$ variability are almost perfectly anticorrelated, representing the dominance of vertical structure in determining the redistribution coefficient κ_r^T. Here, $\kappa_r^T = -0.0210$, $\partial_z\Theta/\partial_z\mathrm{DIC} = -0.0208$.

Appendix B: Merging one and two step estimates

Our estimation technique assumes that the relationship between short timescale changes is dominated by circulation variability. However, at the surface, changes in salinity and $\mathrm{C_{nat}}$ are instead dominated by freshwater fluxes: an excess of evaporation over precipitation will increase concentrations of salt and $\mathrm{C_{nat}}$, coupling changes in the two. This leads to changes which are properly described as excess salinity being partitioned into redistributed salinity.

To account for this, we use a two step estimation process. As we note, we may combine Equations 7 & 8 in order to estimate redistributed salinity from redistributed temperature, or vice versa. We therefore estimate excess salinity at the surface as

$$\Delta S_r = \kappa_r^{\mathrm{T-S}} \times \Delta\Theta_r, \tag{B1}$$

where $\kappa_r^{\mathrm{T-S}}$ is an estimate of the local slope of the temperature-salinity curve, produced in the same fashion as our previous estimates. We refer to this estimate of surface excess salinity as a two step estimate.

We then merge the two estimates using a sigmoidal weighting scheme based on depth. Our simulations use 64 vertical levels, with the 20th level corresponding to approximately 200m. Denoting the $\mathrm{i^{th}}$ vertical level z_i, the one step estimate as S_1 and the two step estimate as S_2, we calculate our final estimate of salinity redistribution, S, as

$$S = S_1 \times \sigma\left(\frac{z_i + 20}{2}\right) + S_2 \times \left(1 - \sigma\left(\frac{z_i + 20}{2}\right)\right), \tag{B2}$$

where $\sigma(z)$ is the sigmoid function:

$$\sigma(z) = \frac{1}{1 + e^{-z}} \tag{B3}$$

Appendix C: Gamma Factor

Figure C1 shows the γ factor over our full run. It increases from 0 at the beginning of the run to 0.117 by 2099. We perform smoothing as in the late 19^{th} and early 20^{th} century, $\mathrm{C_{anth}}$ inventories are small and so large corrections are necessary to perfectly correct a small amount of C_{sat} outgassing: smoothing removes this effectively. By the 21st century, C_{anth} inventories are large enough that smoothing has little effect. Finally, we note that the γ factor does not begin to increase significantly until the late 20th century, approximately the same time that globally integrated ocean heat content begins to increase. Thus, to first order, γ corrects for C_{sat} outgassing due to ocean warming.

Author contributions. CT designed the technique for temperature decomposition, and EM realised the extensibility to salinity. All authors contributed to interpretation and writing the manuscript.

Competing interests. The authors declare no competing interests

Acknowledgements. We would like to thank Matthew Couldrey for kindly allowing us to use his simulations for this research. EM, PB were supported by Natural Environment Research Council grant NE/P019293/1 (TICTOC) CT was supported by the Natural Environmental Research Council [grant number NE/L002531/1]

References

Antonov, J. I., Levitus, S., and Boyer, T. P.: Steric sea level variations during 1957–1994: Importance of salinity, Journal of Geophysical Research: Oceans, 107, SRF 14–1–SRF 14–8, https://doi.org/https://doi.org/10.1029/2001JC000964, 2002.

Banks, H. T. and Gregory, J. M.: Mechanisms of ocean heat uptake in a coupled climate model and the implications for tracer based predictions of ocean heat uptake, Geophysical Research Letters, 33, https://doi.org/https://doi.org/10.1029/2005GL025352, 2006.

Bindoff, N. L. and Mcdougall, T. J.: Diagnosing Climate Change and Ocean Ventilation Using Hydrographic Data, Journal of Physical Oceanography, 24, 1137 – 1152, https://doi.org/10.1175/1520-0485(1994)024<1137:DCCAOV>2.0.CO;2, 1994.

Bopp, L., Lévy, M., Resplandy, L., and Sallée, J. B.: Pathways of anthropogenic carbon subduction in the global ocean, Geophysical Research Letters, 42, 6416–6423, https://doi.org/https://doi.org/10.1002/2015GL065073, 2015.

Bronselaer, B. and Zanna, L.: Heat and carbon coupling reveals ocean warming due to circulation changes, Nature, 584, 227–233, https://doi.org/10.1038/s41586-020-2573-5, 2020.

Caesar, L., Rahmstorf, S., Robinson, A., Feulner, G., and Saba, V.: Observed fingerprint of a weakening Atlantic Ocean overturning circulation, Nature, 556, 191–196, https://doi.org/10.1038/s41586-018-0006-5, 2018.

Church, J., Clark, P., Cazenave, A., Gregory, J., Jevrejeva, S., Levermann, A., Merrifield, M., Milne, G., Nerem, R., Nunn, P., Payne, A., Pfeffer, W., Stammer, D., and Unnikrishnan, A.: Sea Level Change, in: Climate Change 2013: The Physical Science Basis. Contribution of Working Group I to the Fifth Assessment Report of the Intergovernmental Panel on Climate Change, edited by Stocker, T., Qin, D., Plattner, G.-K., Tignor, M., Allen, S., Boschung, J., Nauels, A., Xia, Y., Bex, V., and Midgley, P., pp. 1137–1216, Cambridge University Press, https://doi.org/10.1017/CBO9781107415324.026, section: 13 Type: Book Section, 2013.

Church, J. A., White, N. J., Konikow, L. F., Domingues, C. M., Cogley, J. G., Rignot, E., Gregory, J. M., van den Broeke, M. R., Monaghan, A. J., and Velicogna, I.: Revisiting the Earth's sea-level and energy budgets from 1961 to 2008, Geophysical Research Letters, 38, https://doi.org/https://doi.org/10.1029/2011GL048794, 2011.

Collins, W. J., Bellouin, N., Doutriaux-Boucher, M., Gedney, N., Halloran, P., Hinton, T., Hughes, J., Jones, C. D., Joshi, M., Liddicoat, S., Martin, G., O'Connor, F., Rae, J., Senior, C., Sitch, S., Totterdell, I., Wiltshire, A., and Woodward, S.: Development and evaluation of an Earth-System model – HadGEM2, Geoscientific Model Development, 4, 1051–1075, https://doi.org/10.5194/gmd-4-1051-2011, 2011.

Couldrey, M. P., Oliver, K. I. C., Yool, A., Halloran, P. R., and Achterberg, E. P.: On which timescales do gas transfer velocities control North Atlantic CO2 flux variability?, Global Biogeochemical Cycles, 30, 787–802, https://doi.org/https://doi.org/10.1002/2015GB005267, 2016.

Couldrey, M. P., Oliver, K. I. C., Yool, A., Halloran, P. R., and Achterberg, E. P.: Drivers of 21^{st} Century carbon cycle variability in the North Atlantic Ocean, Biogeosciences Discussions, 2019, 1–33, https://doi.org/10.5194/bg-2019-16, 2019.

Desbruyères, D., McDonagh, E. L., King, B. A., and Thierry, V.: Global and Full-Depth Ocean Temperature Trends during the Early Twenty-First Century from Argo and Repeat Hydrography, Journal of Climate, 30, 1985 – 1997, https://doi.org/10.1175/JCLI-D-16-0396.1, 2017.

Durack, P. J. and Wijffels, S. E.: Fifty-Year Trends in Global Ocean Salinities and Their Relationship to Broad-Scale Warming, Journal of Climate, 23, 4342 – 4362, https://doi.org/10.1175/2010JCLI3377.1, 2010.

Firing, Y. L., McDonagh, E. L., King, B. A., and Desbruyères, D. G.: Deep temperature variability in Drake Passage, Journal of Geophysical Research: Oceans, 122, 713–725, https://doi.org/https://doi.org/10.1002/2016JC012452, 2017.

Goodwin, P., Williams, R. G., and Ridgwell, A.: Sensitivity of climate to cumulative carbon emissions due to compensation of ocean heat and carbon uptake, Nature Geoscience, 8, 29–34, https://doi.org/10.1038/ngeo2304, 2015.

Gould, W. J. and Cunningham, S. A.: Global-scale patterns of observed sea surface salinity intensified since the 1870s, Communications Earth & Environment, 2, 76, https://doi.org/10.1038/s43247-021-00161-3, 2021.

Gregory, J. M., Bouttes, N., Griffies, S. M., Haak, H., Hurlin, W. J., Jungclaus, J., Kelley, M., Lee, W. G., Marshall, J., Romanou, A., Saenko, O. A., Stammer, D., and Winton, M.: The Flux-Anomaly-Forced Model Intercomparison Project (FAFMIP) contribution to CMIP6: investigation of sea-level and ocean climate change in response to CO_2 forcing, Geoscientific Model Development, 9, 3993–4017, https://doi.org/10.5194/gmd-9-3993-2016, 2016.

Gruber, N.: Warming up, turning sour, losing breath: ocean biogeochemistry under global change, Philosophical Transactions of the Royal Society A: Mathematical, Physical and Engineering Sciences, 369, 1980–1996, https://doi.org/10.1098/rsta.2011.0003, 2011.

Gruber, N., Sarmiento, J. L., and Stocker, T. F.: An improved method for detecting anthropogenic CO2 in the oceans, Global Biogeochemical Cycles, 10, 809–837, https://doi.org/https://doi.org/10.1029/96GB01608, 1996.

Hall, T. M., Haine, T. W. N., and Waugh, D. W.: Inferring the concentration of anthropogenic carbon in the ocean from tracers, Global Biogeochemical Cycles, 16, 78–1–78–15, https://doi.org/https://doi.org/10.1029/2001GB001835, 2002.

Hetzinger, S., Halfar, J., Zajacz, Z., and Wisshak, M.: Early start of 20th-century Arctic sea-ice decline recorded in Svalbard coralline algae, Geology, 47, 963–967, https://doi.org/10.1130/G46507.1, 2019.

Hinkel, J., Lincke, D., Vafeidis, A. T., Perrette, M., Nicholls, R. J., Tol, R. S. J., Marzeion, B., Fettweis, X., Ionescu, C., and Levermann, A.: Coastal flood damage and adaptation costs under 21st century sea-level rise, Proceedings of the National Academy of Sciences, 111, 3292–3297, https://doi.org/10.1073/pnas.1222469111, 2014.

Johns, W. E., Baringer, M. O., Beal, L. M., Cunningham, S. A., Kanzow, T., Bryden, H. L., Hirschi, J. J. M., Marotzke, J., Meinen, C. S., Shaw, B., and Curry, R.: Continuous, Array-Based Estimates of Atlantic Ocean Heat Transport at 26.5°N, Journal of Climate, 24, 2429 – 2449, https://doi.org/10.1175/2010JCLI3997.1, 2011.

Katavouta, A., Williams, R. G., Goodwin, P., and Roussenov, V.: Reconciling Atmospheric and Oceanic Views of the Transient Climate Response to Emissions, Geophysical Research Letters, 45, 6205–6214, https://doi.org/https://doi.org/10.1029/2018GL077849, 2018.

Khatiwala, S., Visbeck, M., and Cane, M. A.: Accelerated simulation of passive tracers in ocean circulation models, Ocean Modelling, 9, 51–69, https://doi.org/https://doi.org/10.1016/j.ocemod.2004.04.002, 2005.

Khatiwala, S., Tanhua, T., Mikaloff Fletcher, S., Gerber, M., Doney, S. C., Graven, H. D., Gruber, N., McKinley, G. A., Murata, A., Ríos, A. F., and Sabine, C. L.: Global ocean storage of anthropogenic carbon, Biogeosciences, 10, 2169–2191, https://doi.org/10.5194/bg-10-2169-2013, 2013.

Lauvset, S. K., Key, R. M., Olsen, A., van Heuven, S., Velo, A., Lin, X., Schirnick, C., Kozyr, A., Tanhua, T., Hoppema, M., Jutterström, S., Steinfeldt, R., Jeansson, E., Ishii, M., Perez, F. F., Suzuki, T., and Watelet, S.: A new global interior ocean mapped climatology: the $1^\circ \times 1^\circ$ GLODAP version 2, Earth System Science Data, 8, 325–340, https://doi.org/10.5194/essd-8-325-2016, 2016.

Levang, S. J. and Schmitt, R. W.: Centennial Changes of the Global Water Cycle in CMIP5 Models, Journal of Climate, 28, 6489 – 6502, https://doi.org/10.1175/JCLI-D-15-0143.1, 2015.

Lowe, J. A. and Gregory, J. M.: Understanding projections of sea level rise in a Hadley Centre coupled climate model, Journal of Geophysical Research: Oceans, 111, https://doi.org/https://doi.org/10.1029/2005JC003421, 2006.

MacDougall, A. H. and Friedlingstein, P.: The Origin and Limits of the Near Proportionality between Climate Warming and Cumulative CO 2 Emissions , Journal of Climate, 28, 4217–4230, https://doi.org/10.1175/jcli-d-14-00036.1, 2015.

Madec, G.: NEMO ocean engine, https://doi.org/10.5281/zenodo.1464816, 2008.

Madec, G. and Imbard, M.: A global ocean mesh to overcome the North Pole singularity, Climate Dynamics, 12, 381–388, 1996.

Martin, T. H. D. T. G. M., Bellouin, N., Collins, W. J., Culverwell, I. D., Halloran, P. R., Hardiman, S. C., Hinton, T. J., Jones, C. D., McDonald, R. E., McLaren, A. J., O'Connor, F. M., Roberts, M. J., Rodriguez, J. M., Woodward, S., Best, M. J., Brooks, M. E., Brown, A. R., Butchart, N., Dearden, C., Derbyshire, S. H., Dharssi, I., Doutriaux-Boucher, M., Edwards, J. M., Falloon, P. D., Gedney, N., Gray, L. J., Hewitt, H. T., Hobson, M., Huddleston, M. R., Hughes, J., Ineson, S., Ingram, W. J., James, P. M., Johns, T. C., Johnson, C. E., Jones, A., Jones, C. P., Joshi, M. M., Keen, A. B., Liddicoat, S., Lock, A. P., Maidens, A. V., Manners, J. C., Milton, S. F., Rae, J. G. L., Ridley, J. K., Sellar, A., Senior, C. A., Totterdell, I. J., Verhoef, A., Vidale, P. L., and Wiltshire, A.: The HadGEM2 family of Met Office Unified Model climate configurations, Geoscientific Model Development, 4, 723–757, https://doi.org/10.5194/gmd-4-723-2011, 2011.

Mauritzen, C., Melsom, A., and Sutton, R. T.: Importance of density-compensated temperature change for deep North Atlantic Ocean heat uptake, Nature Geoscience, 5, 905–910, https://doi.org/10.1038/ngeo1639, 2012.

McDougall, T. J. and Barker, P. M.: Getting started with TEOS-10 and the Gibbs Seawater (GSW) Oceanographic Toolbox, SCOR/IAPSO WG127, p. 28, 2011.

McKinley, G. A., Fay, A. R., Lovenduski, N. S., and Pilcher, D. J.: Natural Variability and Anthropogenic Trends in the Ocean Carbon Sink, Annual Review of Marine Science, 9, 125–150, https://doi.org/10.1146/annurev-marine-010816-060529, pMID: 27620831, 2017.

Moreau, S., Vancoppenolle, M., Bopp, L., Aumont, O., Madec, G., Delille, B., Tison, J.-L., Barriat, P.-Y., and Goosse, H.: Assessment of the sea-ice carbon pump: Insights from a three-dimensional ocean-sea-ice biogeochemical model (NEMO-LIM-PISCES), Elementa: Science of the Anthropocene, 4, https://doi.org/10.12952/journal.elementa.000122, 000122, 2016.

Oschlies, A., Brandt, P., Stramma, L., and Schmidtko, S.: Drivers and mechanisms of ocean deoxygenation, Nature Geoscience, 11, 467–473, https://doi.org/10.1038/s41561-018-0152-2, 2018.

Pardaens, A. K., Lowe, J. A., Brown, S., Nicholls, R. J., and de Gusmão, D.: Sea-level rise and impacts projections under a future scenario with large greenhouse gas emission reductions, Geophysical Research Letters, 38, https://doi.org/https://doi.org/10.1029/2011GL047678, 2011.

Pierce, D. W., Gleckler, P. J., Barnett, T. P., Santer, B. D., and Durack, P. J.: The fingerprint of human-induced changes in the ocean's salinity and temperature fields, Geophysical Research Letters, 39, https://doi.org/https://doi.org/10.1029/2012GL053389, 2012.

Riahi, K., Rao, S., Krey, V., Cho, C., Chirkov, V., Fischer, G., Kindermann, G., Nakicenovic, N., and Rafaj, P.: RCP 8.5—A scenario of comparatively high greenhouse gas emissions, Climatic Change, 109, 33–57, https://doi.org/10.1007/s10584-011-0149-y, 2011.

Rodgers, K. B., Ishii, M., Frölicher, T. L., Schlunegger, S., Aumont, O., Toyama, K., and Slater, R. D.: Coupling of Surface Ocean Heat and Carbon Perturbations over the Subtropical Cells under Twenty-First Century Climate Change, Journal of Climate, 33, 10 321 – 10 338, https://doi.org/10.1175/JCLI-D-19-1022.1, 2020.

Sabine, C., Feely, R., Gruber, N., Key, R., Lee, K., Bullister, J., Wanninkhof, R., Wong, C., Wallace, D., Tilbrook, B., Millero, F., Peng, T.-H., Kozyr, A., Ono, T., and Rios, A.: The Oceanic Sink for Anthropogenic CO2, Science (New York, N.Y.), 305, 367–71, https://doi.org/10.1126/science.1097403, 2004.

Sathyanarayanan, A., Kohl, A., and Stammer, D.: Ocean Salinity changes in the global ocean under global warming conditions Part 1: Mechanisms in a strong warming scenario, Journal of Climate, pp. 1 – 56, https://doi.org/10.1175/JCLI-D-20-0865.1, 2021.

Schwinger, J., Tjiputra, J. F., Heinze, C., Bopp, L., Christian, J. R., Gehlen, M., Ilyina, T., Jones, C. D., Salas-Mélia, D., Segschneider, J., Séférian, R., and Totterdell, I.: Nonlinearity of ocean carbon cycle feedbacks in CMIP5 earth system models, Journal of Climate, 27, 3869–3888, https://doi.org/10.1175/JCLI-D-13-00452.1, 2014.

Sgubin, G., Swingedouw, D., Drijfhout, S., Hagemann, S., and Robertson, E.: Multimodel analysis on the response of the AMOC under an increase of radiative forcing and its symmetrical reversal, Climate Dynamics, 45, https://doi.org/10.1007/s00382-014-2391-2, 2014.

Skliris, N., Marsh, R., Josey, S. A., Good, S. A., Liu, C., and Allan, R. P.: Salinity changes in the World Ocean since 1950 in relation to changing surface freshwater fluxes, Climate Dynamics, 43, 709–736, https://doi.org/10.1007/s00382-014-2131-7, 2014.

Stott, P. A., Sutton, R. T., and Smith, D. M.: Detection and attribution of Atlantic salinity changes, Geophysical Research Letters, 35, https://doi.org/https://doi.org/10.1029/2008GL035874, 2008.

Terray, L., Corre, L., Cravatte, S., Delcroix, T., Reverdin, G., and Ribes, A.: Near-Surface Salinity as Nature's Rain Gauge to Detect Human Influence on the Tropical Water Cycle, Journal of Climate, 25, 958 – 977, https://doi.org/10.1175/JCLI-D-10-05025.1, 2012.

Thomas, J., Waugh, D., and Gnanadesikan, A.: Relationship between Ocean Carbon and Heat Multidecadal Variability, Journal of Climate, 31, 1467 – 1482, https://doi.org/10.1175/JCLI-D-17-0134.1, 2018.

Timmermann, R., Goosse, H., Madec, G., Fichefet, T., Ethe, C., and Dulière, V.: On the representation of high latitude processes in the ORCA-LIM global coupled sea ice–ocean model, Ocean Modelling, 8, 175–201, 2005.

Touratier, F. and Goyet, C.: Definition, properties, and Atlantic Ocean distribution of the new tracer TrOCA, Journal of Marine Systems, 46, 169–179, https://doi.org/https://doi.org/10.1016/j.jmarsys.2003.11.016, 2004.

Vázquez-Rodríguez, M., Padin, X. A., Ríos, A. F., Bellerby, R. G. J., and Pérez, F. F.: An upgraded carbon-based method to estimate the anthropogenic fraction of dissolved CO_2 in the Atlantic Ocean, Biogeosciences Discussions, 6, 4527–4571, https://doi.org/10.5194/bgd-6-4527-2009, 2009.

Wadhams, P. and Munk, W.: Ocean freshening, sea level rising, sea ice melting, Geophysical Research Letters, 31, https://doi.org/https://doi.org/10.1029/2004GL020039, 2004.

Weaver, A. J., Sedláček, J., Eby, M., Alexander, K., Crespin, E., Fichefet, T., Philippon-Berthier, G., Joos, F., Kawamiya, M., Matsumoto, K., Steinacher, M., Tachiiri, K., Tokos, K., Yoshimori, M., and Zickfeld, K.: Stability of the Atlantic meridional overturning circulation: A model intercomparison, Geophysical Research Letters, 39, https://doi.org/https://doi.org/10.1029/2012GL053763, 2012.

Williams, R. G. and Follows, M. J.: Ocean Dynamics and the Carbon Cycle: Principles and Mechanisms, Cambridge University Press, https://doi.org/10.1017/CBO9780511977817, 2011.

Williams, R. G., Katavouta, A., and Roussenov, V.: Regional Asymmetries in Ocean Heat and Carbon Storage due to Dynamic Redistribution in Climate Model Projections, Journal of Climate, 34, 3907 – 3925, https://doi.org/10.1175/JCLI-D-20-0519.1, 2021.

Winton, M., Griffies, S. M., Samuels, B. L., Sarmiento, J. L., and Frölicher, T. L.: Connecting Changing Ocean Circulation with Changing Climate, Journal of Climate, 26, 2268 – 2278, https://doi.org/10.1175/JCLI-D-12-00296.1, 2013.

Yool, A., Popova, E. E., and Anderson, T. R.: MEDUSA-2.0: an intermediate complexity biogeochemical model of the marine carbon cycle for climate change and ocean acidification studies, Geoscientific Model Development, 6, 1767–1811, https://doi.org/10.5194/gmd-6-1767-2013, 2013.

Zanna, L., Khatiwala, S., Gregory, J. M., Ison, J., and Heimbach, P.: Global reconstruction of historical ocean heat storage and transport, Proceedings of the National Academy of Sciences, 116, 1126–1131, 2019.

Zhu, C. and Liu, Z.: Weakening Atlantic overturning circulation causes South Atlantic salinity pile-up, Nature Climate Change, 10, 998–1003, https://doi.org/10.1038/s41558-020-0897-7, 2020.

Zika, J. D., Skliris, N., Blaker, A. T., Marsh, R., Nurser, A. J. G., and Josey, S. A.: Improved estimates of water cycle change from ocean salinity: the key role of ocean warming, Environmental Research Letters, 13, 074 036, https://doi.org/10.1088/1748-9326/aace42, 2018.

Zika, J. D., Gregory, J. M., McDonagh, E. L., Marzocchi, A., and Clément, L.: Recent Water Mass Changes Reveal Mechanisms of Ocean Warming, Journal of Climate, 34, 3461 – 3479, https://doi.org/10.1175/JCLI-D-20-0355.1, 2021.

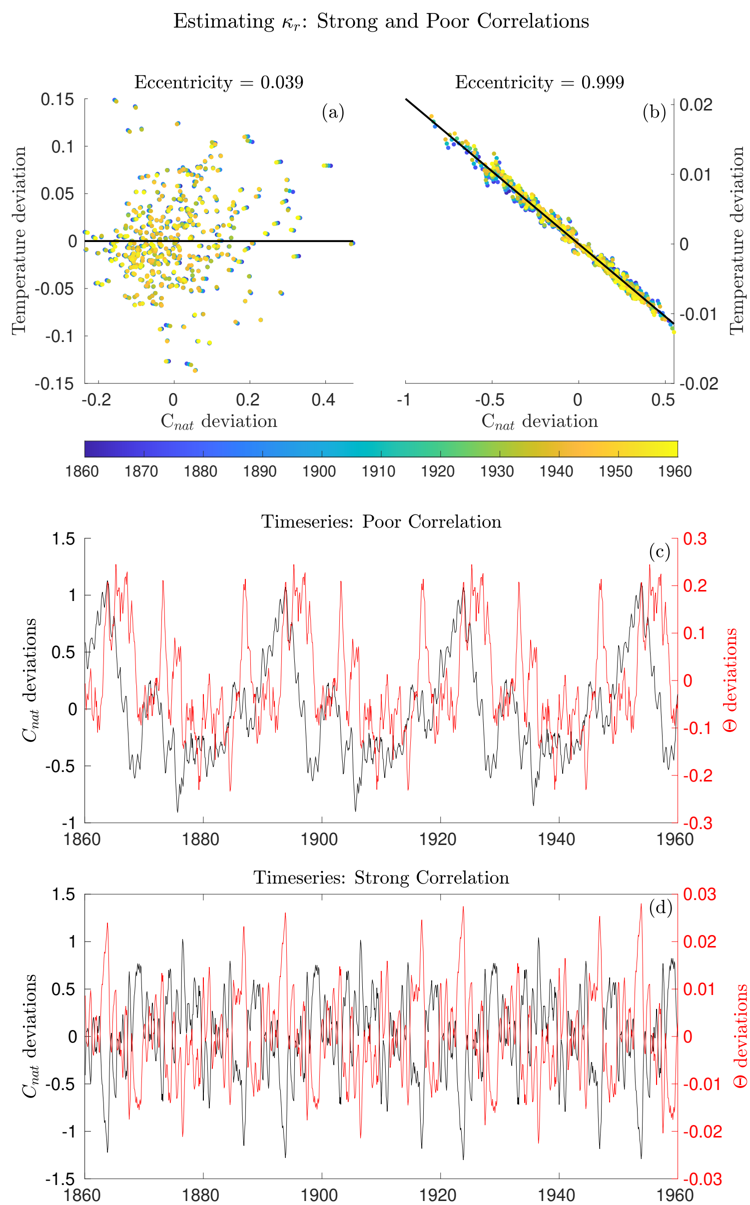

Figure A1. The correlations between $\mathrm{C_{nat}}$ and Θ used to establish a κ_r value, for a poorly correlated point ((a),(c)), and a well correlated point ((b),(d)), in $\Theta - \mathrm{C_{nat}}$ space ((a), (b)), and timeseries of both ((c),(d)). These two points are located at 24N,30W in the Atlantic, at depths of 850 and 1950m. The major axis of the covariance ellipse in panels (a) and (b) is shown in black.

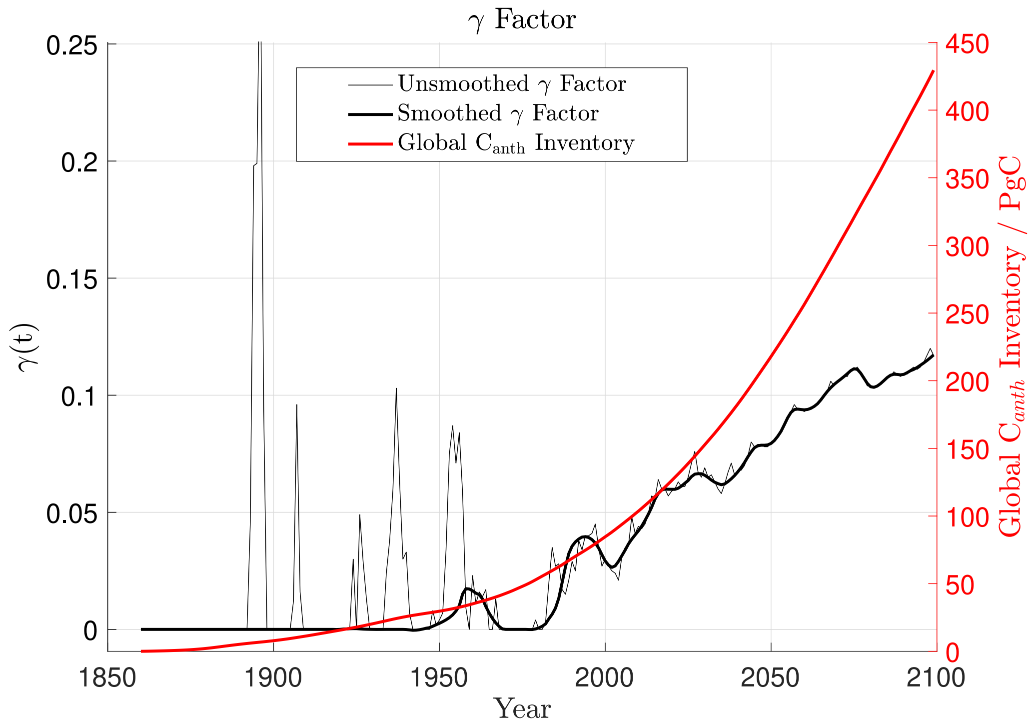

Figure C1. The calculated γ factor (thin black line), smoothed γ factor (thick black line), and global anthropogenic carbon inventory (red line)(.